

A general spectral solver for the axisymmetric Jeans equations: fast galaxy modelling with arbitrary anisotropy

Michele Cappellari[★]

Sub-Department of Astrophysics, Department of Physics, University of Oxford, Denys Wilkinson Building, Keble Road, Oxford, OX1 3RH, UK

Submitted to MNRAS on 2026 January 22

ABSTRACT

Dynamical modelling is a fundamental tool for measuring galaxy masses and density profiles in the era of large integral-field spectroscopic surveys and Bayesian inference. Solutions based on the Jeans equations are popular due to their robustness and computational efficiency. However, traditional semi-analytic Jeans solvers often require restrictive assumptions about the velocity anisotropy to remain computationally tractable. This paper presents a new spectral solver for the axisymmetric Jeans equations designed to overcome these limitations. I first illustrate, using orbit integrations in realistic potentials, that spherical alignment of the velocity ellipsoid is a physically well-motivated approximation for galaxy modelling. The new method employs a spectral technique to solve the Jeans partial differential equations directly. Two design choices are critical for accuracy and speed: (i) solving for the slowly-varying velocity dispersion rather than the rapidly varying pressure, and (ii) imposing a Robin boundary condition to enforce the asymptotic decay on a finite domain. This formulation supports arbitrary anisotropy distributions $\beta(r, \theta)$ while simultaneously increasing computational speed by orders of magnitude compared to standard high-accuracy quadratures. Validated against exact analytic benchmarks, the solver recovers intrinsic moments with sub-percent accuracy. The implementation will be included in the public JAMPy package and is structured to be optimally suited for massive parallelization on specialized hardware such as GPUs, enabling the rigorous exploration of complex parameter spaces.

Key words: methods: data analysis – methods: numerical – techniques: imaging spectroscopy – galaxies: kinematics and dynamics – galaxies: structure – software: data analysis

1 INTRODUCTION

1.1 Dynamical modelling in the era of large surveys

Dynamical models of galaxies are the fundamental scales on which we weigh the Universe. By mapping the gravitational potential, these models allow us to measure the masses of supermassive black holes—essential for understanding feedback processes and galaxy co-evolution—and provide the most direct method to infer the distribution of dark matter by separating it from the luminous stellar component. This decomposition is critical for testing cosmological models and reconstructing the assembly history of galaxies.

The two most widely used techniques for these tasks are orbit-superposition methods (Schwarzschild 1979) and solutions based on the Jeans equations (Jeans 1922). These approaches are highly complementary, with the choice between them often dictated by the quality and quantity of the available data. Schwarzschild models provide a fully general treatment of phase-space structure, but they require high Signal-to-Noise (S/N) spectra to reliably extract the full Line-of-Sight Velocity Distribution (LOSVD) needed to exploit that flexibility. In contrast, Jeans modelling relies only on the lowest-order velocity moments (mean velocity and dispersion). These moments can be measured reliably even from data with moderate S/N ratios or at high redshift where the full LOSVD is inaccessible. This

robustness makes Jeans modelling particularly well-suited for the massive datasets produced by modern Integral Field Spectroscopic (IFS) surveys such as ATLAS^{3D} (Cappellari et al. 2011), CALIFA (Sánchez et al. 2012), SAMI (Croom et al. 2012), and MaNGA (Bundy et al. 2015) (see Cappellari 2016, 2026, for reviews).

Crucially, the simpler assumptions of the Jeans method do not necessarily result in lower accuracy for mass recovery in realistic situations. Leung et al. (2018, fig. 8) benchmarked dynamical models against circular velocities derived from CO gas kinematics in 54 galaxies and found that in the outer regions (0.8 – $1.6R_e$), the measurement errors for the Jeans Anisotropic Multi-Gaussian Expansion (JAM) method were approximately a factor of 1.7 smaller than those for the Schwarzschild method. A similar conclusion was reached by Jin et al. (2019, fig. 4) using numerical simulations; in recovering the enclosed mass within R_e , the scatter in the JAM results was a factor of 1.6 smaller than that of the Schwarzschild technique. Neither study found evidence of systematic bias in the JAM results. These findings confirm that, for mass measurement, the restrictive assumptions of Jeans modelling act as a regulariser that stabilizes the solution against observational noise.

Beyond its robustness, Jeans modelling offers superior computational efficiency. Unlike orbit-superposition methods or N -body simulations, it avoids the costly integration of thousands of orbits. This speed is not merely a matter of convenience; it enables a level of scientific rigor that is often computationally prohibitive for more complex methods. The efficiency of the Jeans approach allows for

[★] E-mail: michele.cappellari@physics.ox.ac.uk

the exploration of vast parameter spaces, facilitating the computation of rigorous Bayesian posteriors and the testing of various physical assumptions—such as different dark matter profiles or anisotropy formulations—to ensure results are statistically well-grounded.

1.2 The mathematical bottleneck of integral transforms

For nearly half a century, the standard approach to solving the axisymmetric Jeans equations has relied on integral transforms. Established by seminal works on axisymmetric semi-isotropic solutions (Satoh 1980; Binney et al. 1990; van der Marel 1991; Emsellem et al. 1994) and spherically-aligned anisotropic solutions (Bacon et al. 1983; Bacon 1985), this strategy reduces two-dimensional partial differential equations (PDEs) to one-dimensional quadratures through judicious changes of variables. This approach has been further refined in the current Jeans Anisotropic Modelling (JAM) method (Cappellari 2008, 2020), as implemented in the JAMPY software packages.¹

While this strategy provides accurate solutions, it imposes strict functional limitations on the galaxy model. The Jeans equation for the radial pressure $\nu\nu_r^2$ constitutes a first-order linear ordinary differential equation. Its general solution requires an *integrating factor* (e.g. Arfken et al. 2013, sec. 7.2), which must be derived analytically to express the final solution as a fast, semi-analytic quadrature. This constraint restricts the anisotropy parameter β to specific forms where the integral $\int(\beta/r)dr$ is analytic. The most common choice is a constant β , which yields a simple power-law integrating factor $r^{2\beta}$, while the most general is the logistic anisotropy of $\lg r$ introduced by Simon et al. (2024b). Any deviation from these restricted forms necessitates the numerical evaluation of nested integrals, which destroys the computational efficiency that makes packages like JAMPY attractive.

The general Jeans equations are PDEs whose mathematical form is analogous to the Euler equations for fluid dynamics; indeed, Jeans (1922) originally referred to them as the “hydrodynamical equation of motions of stars.” One might therefore expect that numerical techniques common in fluid dynamics, such as finite differences or finite elements, would suffice. However, brute-force implementations of these methods struggle to achieve high accuracy and efficiency simultaneously, given the extreme dynamic range of galaxy models. Consequently, such approaches have remained confined to niche theoretical applications. I identified only a handful of studies exploring alternative PDE solution techniques, such as a finite-difference scheme in spheroidal coordinates (Evans 1990) or the method of lines for equations with general velocity ellipsoid alignment (Yurin & Springel 2014); to my knowledge, these have never been employed for the dynamical modelling of real galaxies.

Furthermore, even spectral methods—the focus of this paper—fail if applied without careful formulation. In my initial attempts using spectral collocation to solve for the standard pressure term $\nu\nu_r^2$, I found that because the stellar tracer density ν typically declines by many orders of magnitude from the galaxy centre to the outskirts, a polynomial basis struggles to approximate such a rapidly varying function. Using a finite number of terms, these implementations are either insufficiently accurate or require an excessive number of basis functions, leading to a loss of the very efficiency they sought to provide.

1.3 A new spectral solver

The breakthrough presented in this paper is a specific reformulation of the Jeans problem that overcomes the mathematical bottlenecks described above. I demonstrate that a spectral method can achieve fast exponential convergence, provided two critical design choices are made:

(i) **Solving for the velocity dispersion $\overline{v_r^2}$ rather than the pressure $\nu\nu_r^2$.** As detailed in Section 2.3, while the tracer density ν varies by many orders of magnitude across a galaxy, the velocity dispersion $\overline{v_r^2}$ is a relatively slowly varying function. Solving for this smooth variable allows the spectral representation to be extremely compact, requiring fewer basis functions to achieve high precision.

(ii) **Adopting a Robin boundary condition on a truncated $\log(r)$ radial grid.** As discussed in Section 3.2, standard Dirichlet boundary conditions ($\overline{v_r^2} = 0$) imposed at a finite radius introduce truncation errors that saturate convergence. Conversely, mapping the domain to infinity is often numerically unstable for Multi-Gaussian Expansion (MGE) models (Emsellem et al. 1994; Cappellari 2002) due to the arithmetic underflow of Gaussian densities. The adoption of a Robin condition ($r\partial S/\partial r + \gamma S = 0$) accurately mimics the asymptotic Keplerian behavior of the potential, allowing the method to achieve machine precision even with a finite, truncated grid.

The practical implications of this reformulation are profound. Using the same modest number of grid points currently employed in JAMPY (typically 20×10), our method achieves higher accuracy than the standard JAM quadrature while recovering the solution at a computational speed up to two orders of magnitude faster.

This performance leap is accompanied by the removal of the physical constraints inherent to previous integral-based methods. Our approach handles completely general anisotropy distributions $\beta(r, \theta)$ —for which no analytic integrating factor exists—without any additional computational cost. Such speed and flexibility are essential for modern scientific rigor; they facilitate the exploration of vast parameter spaces, the computation of rigorous Bayesian posteriors, and the systematic testing of different physical assumptions. Furthermore, the method’s structure is naturally suited for massive parallelization on GPUs. These properties suggest that a properly formulated spectral method provides a superior standard for the next generation of dynamical modelling, moving beyond the limitations of traditional integral transforms.

The paper is organized as follows. Section 2 presents the theoretical framework, justifying the spherical alignment assumption and deriving the master equation for the velocity dispersion. Section 3 details the spectral solver algorithm, highlighting the critical role of the Robin boundary condition and the method for spectral interpolation. Section 4 provides the implementation formulas for MGE models. Section 5 validates the solver against exact analytic solutions and benchmarks its performance. Finally, Section 6 summarizes the conclusions.

2 THE SPHERICALLY ALIGNED JEANS FRAMEWORK

2.1 Spherical alignment: the simplest realistic choice

To obtain a unique solution for the axisymmetric Jeans equations, one must assume an orientation for the velocity ellipsoid. While historical treatments have often focused on alignment within cylindrical (Cappellari 2008) or prolate spheroidal coordinates (Dejonghe & de Zeeuw 1988; Evans & Lynden-Bell 1991; Arnold 1995; van de

¹ <https://pypi.org/project/jampy/>

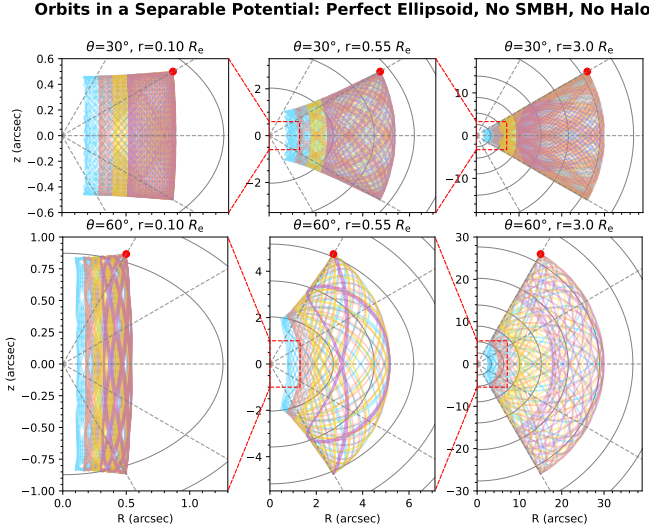


Figure 1. Comparison of orbital envelopes in a separable potential versus a realistic galaxy potential. **Left:** Orbits in a Perfect Ellipsoid potential (de Zeeuw 1985). The orbital boundaries rigidly follow prolate spheroidal coordinates (dashed lines), forcing the velocity ellipsoid to become cylindrically aligned in the core. **Right:** Orbits in a realistic multi-component potential (Sérsic 1968 $n = 4$ bulge + NFW halo Navarro et al. 1996 + Supermassive Black Hole). While the orbits do not strictly follow a single coordinate system, their envelopes are remarkably well approximated by spherical coordinates (dashed lines) at all radii, from the BH-dominated centre ($0.1R_e$) to the halo-dominated outskirts ($3R_e$). This justifies the use of spherically aligned velocity ellipsoids for modelling real galaxies.

Ven et al. 2003), a closer examination of orbital structure in realistic potentials suggests that spherical alignment (Bacon et al. 1983, 1995; Cappellari 2020) holds a unique, physically motivated position for describing real galaxies.

The theoretical baseline for velocity ellipsoid alignment was established by Eddington (1915), who noted that in separable potentials, the principal axes of the velocity ellipsoid align with the coordinate system because the orbital motion decomposes into independent oscillations with zero covariance. This behavior is strictly realized in Stäckel potentials, such as the Perfect Ellipsoid (de Zeeuw 1985). In these systems, orbits rigidly respect a single global coordinate system. As they approach the core, the defining prolate spheroidal coordinates degenerate into cylinders, forcing the velocity ellipsoid into a cylindrical orientation (see Fig. 1, left panel).

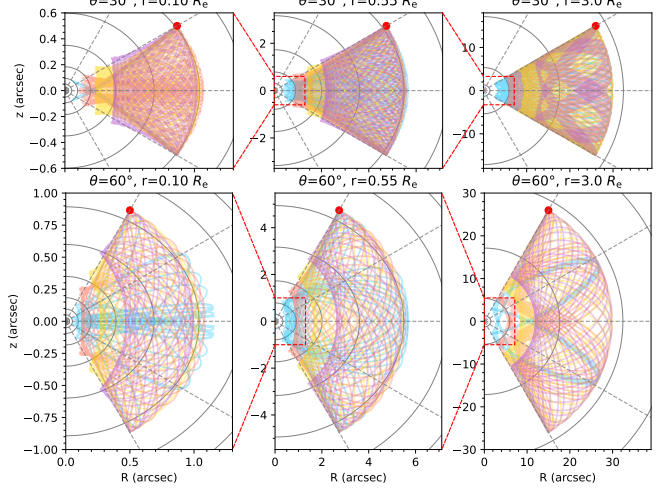
However, real galaxies are significantly more complex. I examine the orbital behavior in a realistic, multi-component potential consisting of a Sérsic (1968) $n = 4$ bulge, an NFW (Navarro et al. 1996) halo, and a supermassive black hole. Fig. 1 (right panel) illustrates the envelopes of regular orbits launched at different inclinations ($\theta = 30^\circ$ and 60°) across three orders of magnitude in radius, from the black-hole dominated nucleus ($0.1R_e$) to the halo-dominated outskirts ($3R_e$).

Two key features emerge from this orbital experiment:

(i) **Local vs. Global Coordinates:** While the boundary of any *individual* orbit may exhibit a slight curvature reminiscent of prolate spheroidal coordinates—showing a small ‘bend’ toward the horizontal near the turning points—this effect is local. As is well known, and evident in the zoomed panels of Fig. 1, these boundaries do not share a common focal distance. Unlike Stäckel potentials, where a single coordinate system defines all motions, real potentials require a ‘Stäckel fudge’ (Binney 2012) where the effective coordinate system varies from orbit to orbit. This concept is central to action-based modelling in software like GALPy (e.g., Bovy 2015) and AGAMA (Vasiliev 2019).

(ii) **Radial Alignment of Turning Points:** Most crucially, the ‘corners’ of the regular orbits (the extrema where radial and angular velocities vanish) align remarkably well with lines of constant spheri-

Orbits in a Realistic Galaxy Potential: Sérsic, SMBH, and NFW Halo



cal polar angle (dashed grey lines) across all scales. Whether deep in the potential well of the black hole or far out in the dark matter halo, the overall motion is dominated by radial oscillation bounded by these constant angular sectors.

Consequently, while the velocity ellipsoid of real galaxies cannot be globally described by any simple coordinate system, like spherical, spheroidal, or cylindrical (Evans et al. 2016), spherical alignment represents the most robust global approximation. It captures the fundamental radial nature of the orbital envelopes observed in Fig. 1 without imposing the artificial constraints that force unphysical cylindrical alignment in the core of separable models. This theoretical expectation is supported by *Gaia* studies (Gaia Collaboration et al. 2016), which are the only ones currently able to measure the ellipsoid orientation in a direct manner, from 6-dim phase space coordinates. These have found that the velocity ellipsoid is well approximated by spherical polar alignment in both the outer stellar halo (Wegg et al. 2019) and the disc region (Everall et al. 2019; Hagen et al. 2019). See the review by Hunt & Vasiliev (2025, sec. 3.4) for a comprehensive discussion of the observational evidence.

Thus, I adopt spherically aligned velocity ellipsoids not merely for mathematical convenience, but because they provide a superior description of the phase-space structure in realistic, non-integrable galactic potentials.

Finally, I emphasize that the spectral formalism presented here, is not mathematically restricted to the spherically aligned case. Unlike semi-analytic quadrature approaches, which rely on specific integrability conditions for efficiency, the spectral method can be applied with equal ease to the Jeans equations with *any* alignment. This includes cylindrically aligned models (JAM_{cyl}; Cappellari 2008), alignment in fixed prolate spheroidal coordinates (Dejonghe & de Zeeuw 1988; Evans & Lynden-Bell 1991; Arnold 1995; van de Ven et al. 2003), or a velocity ellipsoid with a generic tilt specified by an arbitrary function (e.g. Yurin & Springel 2014). One merely needs to rewrite the corresponding PDEs derived in those references, with minimal changes to the implementation. However, given the physical status of spherical alignment discussed above, I consider it the most appropriate

standard for general applications and restrict the formulations in this paper to this case.

2.2 Assumptions and general equations

I adopt a spherical polar coordinate system (r, θ, ϕ) , where the symmetry axis of the galaxy aligns with the z -axis ($\theta = 0$). The spatial domain covers the radial range $r \in [r_{\min}, r_{\max}]$ and the polar angle $\theta \in [0, \pi/2]$. The dynamics of the tracer population are governed by the Jeans equations under the following three fundamental assumptions:

- (i) **Steady state:** The system is time-independent ($\partial/\partial t = 0$).
- (ii) **Axisymmetry:** The density and potential are symmetric about the z -axis ($\partial/\partial\phi = 0$).
- (iii) **Spherical alignment:** The velocity ellipsoid is aligned with the spherical coordinate directions. This implies that the off-diagonal moments of the velocity dispersion tensor vanish in these coordinates ($\overline{v_r v_\theta} = \overline{v_r v_\phi} = \overline{v_\theta v_\phi} = 0$).

Under these assumptions, the two non-trivial Jeans equations can be written as (e.g., [de Zeeuw et al. 1996](#), eq. 2.4):

$$\frac{\partial(\overline{v v_r^2})}{\partial r} + \frac{2\overline{v v_r^2} - \overline{v v_\theta^2} - \overline{v v_\phi^2}}{r} = -v \frac{\partial \Phi}{\partial r}, \quad (1)$$

$$\frac{\partial(\overline{v v_\theta^2})}{\partial \theta} + \frac{\overline{v v_\theta^2} - \overline{v v_\phi^2}}{\tan \theta} = -v \frac{\partial \Phi}{\partial \theta}, \quad (2)$$

where $v(r, \theta)$ represents the tracer density and $\Phi(r, \theta)$ denotes the total gravitational potential.

To close this system, I define the anisotropy parameter as:

$$\beta(r, \theta) \equiv 1 - \frac{\overline{v_\theta^2}}{\overline{v_r^2}}. \quad (3)$$

A key feature of the spectral method presented here is that, unlike traditional quadrature-based approaches, I allow β to vary generally as a function of both radius r and polar angle θ . By substituting $\overline{v_\theta^2} = (1 - \beta)\overline{v_r^2}$ into [equation \(1\)](#) and [equation \(2\)](#), the equations become (e.g., [Bacon et al. 1983](#), eqs. 1 and 2):

$$\frac{\partial(\overline{v v_r^2})}{\partial r} + \frac{(1 + \beta)\overline{v v_r^2} - \overline{v v_\phi^2}}{r} = -v \frac{\partial \Phi}{\partial r}, \quad (4)$$

$$\frac{\partial[(1 - \beta)\overline{v v_r^2}]}{\partial \theta} + \frac{(1 - \beta)\overline{v v_r^2} - \overline{v v_\phi^2}}{\tan \theta} = -v \frac{\partial \Phi}{\partial \theta}. \quad (5)$$

By solving for the radial and angular components simultaneously, this framework provides a self-consistent description of the radial $\overline{v_r^2}$ and azimuthal second moment $\overline{v_\phi^2}$ for any given anisotropy and mass distribution.

As is typical with the Jeans equations, the resulting solution is not guaranteed to be physically realizable; that is, it may not necessarily correspond to a non-negative distribution function. Furthermore, the model should be viewed as an approximation, given that the velocity ellipsoids of real galaxies are never perfectly aligned with a single coordinate system, as argued in [Section 2.1](#).

2.3 Solving for the velocity moments in logarithmic coordinates

In traditional Jeans modelling, it is customary to solve for the “pressure” term $\overline{v v_r^2}$. However, in galactic systems, the tracer density v typically spans many orders of magnitude from the nucleus to the outskirts,

whereas the velocity dispersion $\overline{v_r^2}$ varies only by a factor of a few. A numerical scheme solving for $\overline{v v_r^2}$ must therefore capture an enormous dynamic range, which can lead to a significant loss of precision in the outer regions. To circumvent this, I minimize the dynamic range of the solution by solving directly for the intrinsic second moment $\overline{v_r^2}$. Furthermore, to handle the large radial scales efficiently, I utilize the logarithmic radial coordinate $x = \ln r$.

I begin by eliminating the azimuthal second moment $\overline{v v_\phi^2}$ between the radial and angular Jeans equations ([equation \(4\)](#) and [equation \(5\)](#)). By combining these equations and utilizing the vector identity:

$$r \cos \theta \frac{\partial \Phi}{\partial r} - \sin \theta \frac{\partial \Phi}{\partial \theta} = r \frac{\partial \Phi}{\partial z}, \quad (6)$$

the right-hand side is reduced to a compact form involving the vertical gradient of the potential, which is computationally efficient to evaluate for MGE models. This procedure generalizes the approach of [Bacon et al. \(1983, eq. 3\)](#) to allow for a general anisotropy $\beta(r, \theta)$. Throughout the derivation, I multiply the equations by $\cos \theta$ to eliminate the singularity of the $\tan \theta$ term at the equatorial plane ($\theta = \pi/2$), ensuring that all terms remain finite. The resulting partial differential equation (PDE) for the radial pressure $\overline{v v_r^2}$ is:

$$-\cos \theta \frac{\partial(\overline{v v_r^2})}{\partial \ln r} + \sin \theta \frac{\partial[(1 - \beta)\overline{v v_r^2}]}{\partial \theta} - 2\beta \cos \theta (\overline{v v_r^2}) = v r \frac{\partial \Phi}{\partial z}. \quad (7)$$

To transform this into an equation for the velocity dispersion, I expand the derivatives of the product terms using the product rule and divide the entire equation by the tracer density v . This yields a linear first-order transport PDE for $\overline{v_r^2}$ with source and reaction terms:

$$-\cos \theta \frac{\partial \overline{v_r^2}}{\partial \ln r} + (1 - \beta) \sin \theta \frac{\partial \overline{v_r^2}}{\partial \theta} + C(r, \theta) \overline{v_r^2} = r \frac{\partial \Phi(R, z)}{\partial z}. \quad (8)$$

The coefficient $C(r, \theta)$ accounts for the spatial gradients of the density and anisotropy:

$$C(r, \theta) = \sin \theta \left[(1 - \beta) \frac{\partial \ln v}{\partial \theta} - \frac{\partial \beta}{\partial \theta} \right] - \cos \theta \left[\frac{\partial \ln v}{\partial \ln r} + 2\beta \right]. \quad (9)$$

This formulation is regular throughout the domain $\theta \in [0, \pi/2]$ and explicitly accommodates angular variations in anisotropy. As discussed in [Section 1](#), $S \equiv \overline{v_r^2}$ is a smooth function, making it ideal for the spectral solver described in [Section 3](#).

Once the radial dispersion $\overline{v_r^2}$ is obtained, the azimuthal second moment $\overline{v_\phi^2}$ is calculated directly from [equation \(4\)](#):

$$\overline{v_\phi^2} = \overline{v_r^2} \left(1 + \beta + \frac{\partial \ln v}{\partial \ln r} \right) + \frac{\partial \overline{v_r^2}}{\partial \ln r} + \frac{\partial \Phi}{\partial \ln r}. \quad (10)$$

The $\partial \overline{v_r^2} / \partial \ln r$ derivatives, are evaluated spectrally from the previous $\overline{v_r^2}$ solution, to maintain high precision and efficiency.

3 SPECTRAL SOLUTION ALGORITHM

I solve the governing [equation \(8\)](#) using a spectral method. The idea of the method is simple. One assumes the solution can be approximated with polynomials, evaluates the PDE on the polynomials at a grid of collocation points and solves a system to find the unique polynomials that satisfy the PDE at the collocation points.

3.1 Chebyshev collocation and mapping

I implement this approach using a tensor-product Chebyshev collocation spectral method. A clear, practically oriented overview of this method can be found in Trefethen (2000), while the key concepts are also presented in Press et al. (2007, Chapter 20.7). More general treatments are available in Boyd (2001) and Shen et al. (2011).

The physical log-radial domain $x \in [x_{\min}, x_{\max}]$ (where $x = \ln r$) and the angular domain $\theta \in [0, \pi/2]$ are mapped to the spectral domain $(\xi, \eta) \in [-1, 1] \times [-1, 1]$ using the linear transformations:

$$x(\xi) = \frac{x_{\max} - x_{\min}}{2} \xi + \frac{x_{\max} + x_{\min}}{2}, \quad \theta(\eta) = \frac{\pi}{4}(\eta + 1). \quad (11)$$

Given that the governing equations are already formulated in log-coordinates, the derivative operators transform as:

$$\frac{\partial}{\partial \ln r} = \frac{2}{\ln(r_{\max}/r_{\min})} \frac{\partial}{\partial \xi}, \quad \frac{\partial}{\partial \theta} = \frac{4}{\pi} \frac{\partial}{\partial \eta}. \quad (12)$$

I discretise the domain using Chebyshev–Gauss–Lobatto nodes. For N_r radial points and N_θ angular points, the nodes are $\xi_i = -\cos(\pi i / N_r)$ and $\eta_j = -\cos(\pi j / N_\theta)$. The unknown function $\bar{v}_r^2 = S(x, \theta)$ is represented by a vector S_{vec} of size $N_r N_\theta$, formed by flattening the grid values $S_{i,j} = S(x_i, \theta_j)$.

Differentiation is performed using the standard Chebyshev differentiation matrix D (e.g. Trefethen 2000, eq. 6.3–6.5). For $N + 1$ Chebyshev nodes $x_j = \cos(j\pi/N)$ ($j = 0, \dots, N$), the entries of D are:

$$\begin{aligned} D_{00} &= \frac{2N^2 + 1}{6}, & D_{NN} &= -\frac{2N^2 + 1}{6}, \\ D_{jj} &= \frac{-x_j}{2(1 - x_j^2)}, & j &= 1, \dots, N - 1, \\ D_{ij} &= \frac{c_i}{c_j} \frac{(-1)^{i+j}}{x_i - x_j}, & i &\neq j, \end{aligned} \quad (13)$$

where $c_0 = c_N = 2$ and $c_j = 1$ otherwise.

I construct the 1D differentiation matrices D_ξ (size $N_r \times N_r$) and D_η (size $N_\theta \times N_\theta$). The 2D differential operators are then constructed using Kronecker products (\otimes). Due to the general dependence of $\beta(r, \theta)$, the coefficients are not strictly separable. Consequently, I construct the operators by multiplying the derivative matrices with diagonal matrices representing the variable coefficients. While FFT-based methods or separable optimizations could be used, they are not computationally necessary given the small size of the grids (typically 40×30) studied here.

Let I_r and I_θ be identity matrices of size N_r and N_θ , respectively. The terms in equation (8) are discretised as follows:

(i) **Radial term:** $-\cos \theta \frac{\partial S}{\partial \ln r}$

$$L_{\text{rad}} = \text{diag}(-\cos \theta) \left[\frac{2}{\ln(r_{\max}/r_{\min})} D_\xi \otimes I_\theta \right]. \quad (14)$$

(ii) **Angular term:** $(1 - \beta) \sin \theta \frac{\partial S}{\partial \theta}$

$$L_{\text{ang}} = \text{diag}[(1 - \beta) \sin \theta] \left(\frac{4}{\pi} I_r \otimes D_\eta \right). \quad (15)$$

(iii) **Decay term:** CS

$$L_{\text{decay}} = \text{diag}(C). \quad (16)$$

The full discrete operator is $L = L_{\text{rad}} + L_{\text{ang}} + L_{\text{decay}}$. The PDE is thus reduced to the linear system:

$$L S_{\text{vec}} = \mathbf{b}, \quad (17)$$

where \mathbf{b} is the vectorised source term $r(\partial \Phi / \partial z)$. The boundary conditions are subsequently incorporated into this system as described in Section 3.2.

3.2 The boundary conditions

The partial differential equation defined in equation (8) is first-order and linear. As illustrated in fig. 2 of Cappellari (2020), the characteristic curves of this system originate from the outer boundary at infinity and propagate inwards, eventually reaching the equatorial plane at various radii. Consequently, the solution is uniquely determined by the boundary condition at infinity, effectively reducing the problem to a set of initial-value ordinary differential equations (ODEs) integrated along these characteristics.

For this reason, I do not impose boundary conditions in θ . I have verified that adding symmetry boundary conditions (e.g., $\partial \bar{v}_r^2 / \partial \theta = 0$) at the angular boundaries $\theta = 0$ and $\theta = \pi/2$ does not alter the numerical solution, which is consistent with the mathematical structure of the system.

Regarding the radial boundary, the natural physical condition is $\bar{v}_r^2 \rightarrow 0$ as $r \rightarrow \infty$. However, spectral methods generally require either a bounded domain or a mapping to infinity. While a rational function mapping (e.g. Canuto et al. 2007, sec. 8.8.2) can theoretically cover the semi-infinite domain $[0, \infty)$, I found that in practice this leads to poor sampling of the core regions and reduced accuracy. Furthermore, mapping to infinity requires evaluating Multi-Gaussian Expansion (MGE) densities and potentials at extremely large radii where the exponentials underflow to zero, causing numerical instability.

Instead, I adopt a finite radial domain with a large outer boundary r_{\max} (typically $r_{\max} \approx 3 \times \max(\sigma_{\text{MGE}})$). Experiments revealed that simple homogeneous Dirichlet conditions ($\bar{v}_r^2 = 0$) at this finite boundary introduce significant truncation errors that saturate the exponential convergence curve and prevent the method from reaching machine precision (Section 5). While this error can be mitigated by increasing r_{\max} , doing so inefficiently redistributes grid points away from the galaxy centre where kinematic data are typically concentrated.

The proper solution is to impose a Robin boundary condition (e.g. Strauss 2008, sec. 1.4) that mimics the asymptotic behavior of the galaxy. Assuming a local power-law behavior $\bar{v}_r^2 \propto r^{-\gamma}$ near the boundary, we have:

$$\frac{\partial \ln \bar{v}_r^2}{\partial \ln r} \approx -\gamma \Rightarrow \frac{r}{\bar{v}_r^2} \frac{\partial \bar{v}_r^2}{\partial r} = -\gamma. \quad (18)$$

Rearranging this yields the Robin boundary condition:

$$r \frac{\partial \bar{v}_r^2}{\partial r} + \gamma \bar{v}_r^2 = 0. \quad (19)$$

The choice of the Robin parameter γ is physically motivated. Consider the spherical Jeans equation for a constant anisotropy β (Binney & Tremaine 2008, eq. 4.215):

$$\frac{d(\bar{v}_r^2)}{dr} + \frac{2\beta}{r} \bar{v}_r^2 = -\nu \frac{d\Phi}{dr} = -\frac{\nu v_c^2}{r}, \quad (20)$$

where v_c is the circular velocity. If we assume that at large radii the tracer density, the circular velocity squared, and the solution follow power-laws $\nu \propto r^{-\alpha}$, $v_c^2 \propto r^{-k}$, and $\bar{v}_r^2 \propto r^{-\gamma}$, which are all good approximations in the outer parts of real galaxies, substitution into the Jeans equation yields:

$$(\alpha + \gamma - 2\beta) r^{-(\alpha + \gamma + 1)} \propto r^{-(\alpha + k + 1)}. \quad (21)$$

Equating the exponents shows that $\gamma = k$. Remarkably, the asymptotic logarithmic slope of the velocity second moment is determined entirely by the slope of the potential *independently of the tracer slope α* . In

the Keplerian and isotropic limit, this is consistent e.g. with the asymptotic trend for double power-law models (Zhao 1996, eq. 39) and several other special cases (e.g. Hernquist 1990; Tremaine et al. 1994). While derived here for the spherical case, this asymptotic behavior is expected to apply radially to every angle even in non-spherical systems.

In real galaxies, v_c^2 has a limited physical range at large radii: it varies from flat ($k \approx 0$) in dark-matter-dominated halos to Keplerian ($k \approx 1$) for finite-mass systems. This implies a very narrow range of allowed slopes for the Robin BC, namely $0 \leq \gamma \leq 1$. In my tests, I adopt the Keplerian limit $\gamma = 1$, which preserves spectral convergence even for moderate r_{\max} and ensures the solution remains weakly sensitive to small variations in the chosen slope. But I verified that any choice in the physical range produces similar results.

3.3 Recovering the azimuthal velocity dispersion

Once $\overline{v_r^2}$ is determined, the azimuthal second moment $\overline{v_\phi^2}$ is computed using the radial Jeans equation (equation (10)), which remains valid for a general $\beta(r, \theta)$. All terms are evaluated spectrally with minimal additional computational cost. The radial derivative $\partial \overline{v_r^2} / \partial \ln r$ is obtained by applying the operator $D_\xi \otimes I_\theta$ (including the mapping metric) to the solution vector S_{vec} . The radial potential gradient Φ_r is computed via the chain rule, $\Phi_r = \Phi_R \sin \theta + \Phi_z \cos \theta$, using cylindrical potential derivatives; here, Φ_z is reused from the source term of the spectral solver and does not require recomputation.

3.4 Spectral interpolation

To compare the models with observations, I project the intrinsic moments along the line of sight (LOS). A fundamental advantage of the spectral method over finite-difference or discrete quadrature approaches is that it does not merely provide the solution at discrete grid points. Instead, it yields a global functional form for the solution $S(r, \theta)$ expressed as a high-order polynomial. This allows for the evaluation of the smooth solution and its derivatives at any arbitrary location in the domain with spectral accuracy.

I employ barycentric Lagrange interpolation, which is both numerically stable and efficient. For 1D Chebyshev points of the second kind x_k with weights $w_k = (-1)^k \delta_k$ (where $\delta_k = 1/2$ at endpoints and 1 otherwise; Berrut & Trefethen 2004, eq. 5.4), the interpolant is given by (Berrut & Trefethen 2004, eq. 4.2):

$$f(x) \approx \frac{\sum_k \frac{w_k}{x - x_k} f_k}{\sum_k \frac{w_k}{x - x_k}}. \quad (22)$$

For the 2D field $S(r, \theta)$, I perform a tensor-product interpolation. Given a point (r, θ) along the LOS, it is first mapped to spectral coordinates (ξ, η) . I then interpolate along the angular direction η for each radial node to obtain $S_i(\eta)$, and subsequently interpolate these values along the radial direction ξ to obtain $S(\xi, \eta)$.

While barycentric interpolation is computationally more intensive than bilinear interpolation, the latter introduces discretization errors that scale algebraically with grid size, potentially degrading the exponential convergence of the spectral solver. In contrast, barycentric interpolation preserves spectral accuracy, ensuring that the interpolation step does not become the accuracy bottleneck. For applications where maximum speed is critical and moderate accuracy suffices, bilinear interpolation remains a valid alternative.

3.5 Line-of-sight integration

The LOS integration proceeds by defining a coordinate system (x', y', z') , where z' is the coordinate along the LOS. At each sky-plane pixel (x', y') , I integrate quantities such as the tracer density ν and the LOS-weighted second moment $\nu \overline{v_{\text{los}}^2}$ along z' . At each integration step, coordinates are transformed to the galaxy frame (r, θ) , and the intrinsic moments $\overline{v_r^2}, \overline{v_\theta^2}, \overline{v_\phi^2}$ are evaluated via interpolation, projected onto the LOS vector, and summed using a quadrature rule. For this step, I employ the general tensor-projection formalism described in Cappellari (2020, sec. 3).

In my previous implementation (e.g. Cappellari 2020, sec. 6.3), the LOS integral was evaluated over the full domain $(-\infty, \infty)$ using a standard TANH-based quadrature (Schwartz 1969). This approach is efficient where the integrand is smooth; however, the presence of a supermassive black hole creates a singularity in the potential and velocity dispersion at the galaxy centre ($r = 0$). While adaptive quadrature can handle such features, it is ill-suited for the massive parallelisation required by GPU hardware, which relies on fixed instruction sets across threads.

To resolve this without sacrificing accuracy or resorting to a prohibitively large number of fixed points, I optimize the integration by splitting the interval at $z' = 0$ (the point of closest approach to the galaxy centre). This allows the singularity to be treated as a domain endpoint. I apply the “mixed rule” quadrature (Press et al. 2007, Table 4.5.14, third column) to each resulting semi-infinite interval. This rule utilizes the transformation $z' = \exp(t - e^{-t})$, which provides double-exponential (DE) convergence (Takahasi & Mori 1974) at the lower limit ($z' = 0$), effectively neutralizing the central singularity. It maintains a single-exponential fall-off at infinity, which is sufficient because the MGE surface brightness decreases exponentially and typically becomes negligible beyond $\approx 3 \max(\sigma_{\text{MGE}})$. This tailored quadrature allows for high-accuracy integration, achieving errors below the per cent level with as few as 20 points, even for cuspy profiles. By reducing the necessary evaluation points by an order of magnitude, this optimization ensures that the projection step complements the speed of the spectral solver.

3.6 Computing gradients of density and potential

The spectral method presented here is fundamentally general: it solves the governing partial differential equations for any tracer density ν and gravitational potential Φ , provided their gradients can be evaluated at the collocation nodes. The implementation explicitly allows the user to provide arbitrary software functions to compute these gradients. This flexibility represents a significant departure from previous Jeans Anisotropic Modelling (JAM) implementations, which relied entirely on the Multi-Gaussian Expansion (MGE) formalism for both the potential and the density to enable semi-analytic integration.

A typical application of this new capability involves models where an axisymmetric stellar tracer is embedded in a non-stellar gravitational potential, such as a dark matter halo not derived from the stellar density. A popular choice for the total density is the generalized NFW (gNFW; Wyithe et al. 2001) profile, which I employ in the test described in Section 5.2. This setup is frequently utilized in dynamical studies (e.g. Poci et al. 2017; Lu et al. 2024). In such cases, the gravitational force of the total density often has a simple analytic form (Zhao 1996). These analytic gradients can be passed directly to the spectral solver, accelerating the computation and, crucially, avoiding the need to approximate the analytic dark matter profile with a one-dimensional MGE fit.

However, for the stellar component, obtaining an accurate intrin-

sic density from observations requires deprojection of the surface brightness. For this purpose, the MGE method (Emsellem et al. 1994; Cappellari 2002) remains the preferred tool due to its ability to fit complex profiles accurately and deproject them analytically. Consequently, while the solver is general, its integration with MGE components is of primary practical importance. In the following section, I provide the specific formulas required to implement the spectral solver for models where the density and/or potential are described by an MGE.

4 IMPLEMENTATION FOR MGE MODELS

4.1 Tracer density derivatives

I assume the tracer number density ν is the deprojection of a surface brightness parameterised by N Gaussian components. In cylindrical coordinates (R, z) , the density is given by:

$$\nu(R, z) = \sum_{k=1}^N \nu_{0k} \exp \left[-\frac{1}{2\sigma_k^2} \left(R^2 + \frac{z^2}{q_k^2} \right) \right], \quad (23)$$

where ν_{0k} is the central density, σ_k the dispersion, and q_k the intrinsic flattening of the k -th component. In spherical coordinates (r, θ) , substituting $R = r \sin \theta$ and $z = r \cos \theta$, the exponent for each component becomes $-r^2/(2\sigma_k^2)[\sin^2 \theta + (\cos^2 \theta)/q_k^2]$.

The spectral solver requires the logarithmic derivatives of ν . The radial derivative is:

$$\frac{\partial \ln \nu}{\partial \ln r} = -\frac{1}{\nu(R, z)} \sum_{k=1}^N \frac{\nu_k(R, z)}{\sigma_k^2} \left(R^2 + \frac{z^2}{q_k^2} \right), \quad (24)$$

where $\nu_k(R, z)$ represents the density contribution of the k -th component. The angular derivative is derived from the term $\partial_\theta [\sin^2 \theta + \cos^2 \theta/q_k^2] = 2 \sin \theta \cos \theta - 2 \sin \theta \cos \theta/q_k^2 = \sin(2\theta)(1 - 1/q_k^2)$. Thus:

$$\frac{\partial \ln \nu}{\partial \theta} = -\frac{R z}{\nu(R, z)} \sum_{k=1}^N \frac{\nu_k(R, z)}{\sigma_k^2} \left(1 - \frac{1}{q_k^2} \right). \quad (25)$$

4.2 Gravitational potential and forces

The source term of the linear system in equation (8) depends on the vertical potential derivative Φ_z . I assume the potential is generated by a central supermassive black hole of mass M_\bullet and a mass distribution (stars and dark matter) parameterised by an MGE with M components $(\rho_{0j}, \sigma_j, q_j)$. The total potential is $\Phi = \Phi_\bullet + \Phi_{\text{gal}}$.

The black hole contribution is $\Phi_\bullet = -GM_\bullet/r$, with $r = \sqrt{R^2 + z^2}$, yielding the vertical derivative:

$$\frac{\partial \Phi_\bullet}{\partial z} = \frac{GM_\bullet z}{r^3}. \quad (26)$$

For the galaxy potential Φ_{gal} , I adopt the integral expression from Cappellari (2020, eq. 44). To simplify the notation, I define the exponential term:

$$\mathcal{E}_j(R, z, u) \equiv \exp \left[-\frac{1}{2\sigma_j^2} \left(\frac{R^2}{1+u} + \frac{z^2}{q_j^2+u} \right) \right]. \quad (27)$$

The potential is then:

$$\Phi_{\text{gal}}(R, z) = -2\pi G \int_0^\infty \sum_{j=1}^M \frac{\rho_{0j} q_j \sigma_j^2 \mathcal{E}_j(R, z, u)}{(1+u)\sqrt{q_j^2+u}} du. \quad (28)$$

The vertical derivative required for the solver is:

$$\frac{\partial \Phi_{\text{gal}}}{\partial z} = 2\pi G z \int_0^\infty \sum_{j=1}^M \frac{\rho_{0j} q_j \mathcal{E}_j(R, z, u)}{(1+u)(q_j^2+u)^{3/2}} du. \quad (29)$$

As discussed in Cappellari (2020, sec. 6.2), I evaluate these integrals using the double-exponential (DE) quadrature method (Takahasi & Mori 1974; Trefethen & Weideman 2014; Press et al. 2007, sec. 4.5). I apply the change of variable $u = \exp(\frac{\pi}{2} \sinh t)$, which maps $t \in (-\infty, \infty)$ to $u \in (0, \infty)$. In practice, I find that integrating over $t \in (-3.7, 3.7)$ ensures a fractional truncation error below 10^{-13} . This transformation is exceptionally efficient because it forces the integrand to decay double-exponentially at both ends of the interval, allowing the trapezoidal rule to achieve high precision even when the original integrand decays slowly (as $u^{-5/2}$). I have verified that 60 points in t provide 10^{-4} relative precision for all common MGE profiles. The quadrature for all (R, z) coordinates in the grid can be computed with a single vectorized operation, leveraging modern CPU and GPU architectures for optimal performance.

To recover $\overline{v_\phi^2}$ via equation (10), the radial gradient $\partial \Phi / \partial r$ is also required. For the black hole, $\partial \Phi_\bullet / \partial r = GM_\bullet / r^2$. For the galaxy, I combine the cylindrical derivatives using the chain rule: $\Phi_r = (\partial \Phi_{\text{gal}} / \partial R) \sin \theta + (\partial \Phi_{\text{gal}} / \partial z) \cos \theta$. The cylindrical radial derivative is:

$$\frac{\partial \Phi_{\text{gal}}}{\partial R} = 2\pi G R \int_0^\infty \sum_{j=1}^M \frac{\rho_{0j} q_j \mathcal{E}_j(R, z, u)}{(1+u)^2 (q_j^2+u)^{1/2}} du. \quad (30)$$

The total radial force is thus:

$$\frac{\partial \Phi}{\partial r} = \frac{GM_\bullet}{r^2} + \sin \theta \frac{\partial \Phi_{\text{gal}}}{\partial R} + \cos \theta \frac{\partial \Phi_{\text{gal}}}{\partial z}. \quad (31)$$

Both $\partial \Phi_{\text{gal}} / \partial R$ and $\partial \Phi_{\text{gal}} / \partial z$ are computed using the same DE quadrature scheme, ensuring high accuracy and numerical consistency across the spectral grid.

5 TESTS AND BENCHMARKS

In this section, I validate the spectral solver by benchmarking its results against both existing numerical methods and analytic solutions. The primary focus of these comparisons is on the intrinsic velocity moments (v_r^2, v_ϕ^2) . This choice is motivated by the fact that the projection onto the observational plane relies on the established formalism of Cappellari (2020). While I have replaced the original bilinear interpolation with a more precise barycentric spectral scheme (Section 3.4), the underlying geometry of the line-of-sight integration remains unchanged.

Logically, if the intrinsic moments recovered by the spectral solver are correct, the projected observables will be correct by extension. I have explicitly verified this by comparing projected maps from the spectral JAM method against those from the standard quadrature-based JAM; the two approaches yield high-accuracy agreement across the entire sky plane. By focusing the following benchmarks on the intrinsic 3D moments, I provide a more stringent test of the core mathematical breakthrough of this paper: the numerical solution of the Jeans partial differential equations.

5.1 Comparison with the analytic isotropic Satoh solution

Fully analytic solutions are essential for the rigorous benchmarking of any new numerical solver. They provide a ground truth that can be evaluated to machine precision and, unlike discretized models, are

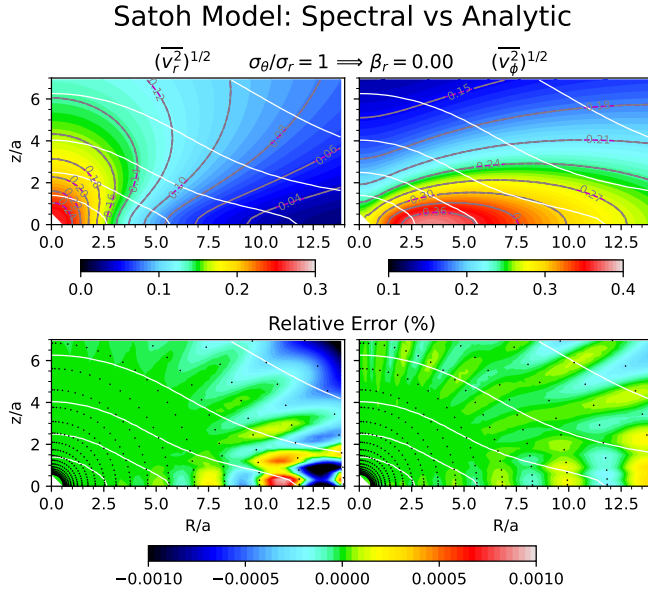


Figure 2. Performance of the spectral JAM solver against the exact analytic isotropic Satoh model ($\beta = 0$). **Top panels:** Maps of the intrinsic radial and azimuthal velocity dispersions, $(v_r^2)^{1/2}$ and $(v_\phi^2)^{1/2}$, computed on a 32×24 grid. **Bottom panels:** Relative percentage error between the spectral and analytic solutions. The residuals are essentially structureless and remain negligible (< 0.2 per cent) throughout the meridional plane.

guaranteed to satisfy the governing equations and boundary conditions exactly. In this first test, I assess the accuracy and convergence properties of the spectral method in isolation, eliminating any uncertainties that might be introduced by the Multi-Gaussian Expansion (MGE) approximation of the density or potential.

I consider the isotropic case of the galaxy model by [Satoh \(1980\)](#). This model is self-consistent and possesses a fully analytic solution for the velocity second moments in the semi-isotropic limit—where the velocity ellipsoid has a circular cross-section in the (R, z) meridional plane ($\sigma_R = \sigma_z$ and $\overline{v_R v_z} = 0$). This corresponds to the solution provided in [Cappellari \(2020\)](#), eqs. 68–69 by setting $\beta_z = 1$. To test the solver’s pure numerical performance, I provide the *exact* analytic gradients of the Satoh potential and tracer density as inputs to the spectral code, rather than their MGE approximations.

The results are presented in [Fig. 2](#) and [Fig. 3](#). [Fig. 2](#) visualizes the solution and the relative errors for a representative grid of size $N_r \times N_\theta = 32 \times 24$. The spectral method recovers the intrinsic moments $(v_r^2)^{1/2}$ and $(v_\phi^2)^{1/2}$ with remarkable fidelity; the relative errors show no significant systematic structure and remain below 0.001 per cent (i.e., 10^{-5}) across the entire meridional plane.

The quantitative convergence is analysed in [Fig. 3](#), which plots the maximum relative error against the number of angular grid points N_θ (while maintaining $N_r = 2N_\theta$). This test highlights the critical role of the boundary conditions discussed in [Section 3.2](#). In spectral methods, accuracy typically exhibits an initial transient regime, followed by exponential convergence once the solution is adequately resolved. However, as shown by the red squares, when a standard Dirichlet boundary condition ($\overline{v_r^2} = 0$) is imposed at the finite outer boundary r_{\max} , the convergence quickly saturates around an error floor of 10^{-3} . This saturation is a direct consequence of the truncation error at the boundary, where the physical solution is small but non-zero.

In contrast, the Robin boundary condition ([equation \(19\)](#)) success-

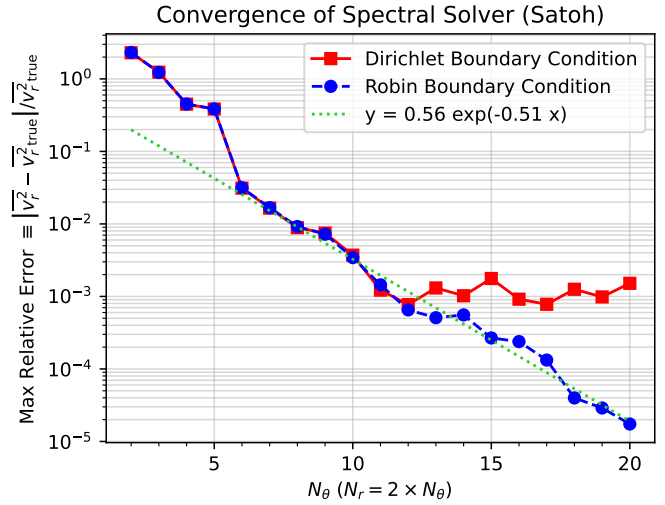


Figure 3. Numerical convergence of the spectral solver as a function of grid resolution. Imposing a Dirichlet boundary condition ($\overline{v_r^2} = 0$) at a finite radius $r_{\max} = 3 \max\{\sigma_k\}$ causes the error to saturate (red solid line with squares). The adoption of a Keplerian Robin boundary condition (blue dashed line with circles) restores exponential convergence, allowing the error to decrease toward machine precision. An exponential fit (green dotted line) to the data for $N_\theta \geq 7$ demonstrates the rapid convergence rate. Remarkably, the method achieves ~ 1 per cent accuracy with a grid as coarse as 14×7 points.

fully eliminates this saturation (blue circles). The error continues to decrease exponentially toward machine precision limits. The convergence is well-fitted by the exponential $y \approx 0.56 \exp(-0.51x)$, demonstrating that the method achieves ~ 1 per cent accuracy with as few as $N_\theta = 7$ angular points (a 14×7 grid). This dramatic efficiency gain over traditional grid-based or quadrature methods is a hallmark of properly formulated spectral techniques.

5.2 Comparison with the analytic isotropic MGE solution

While the Satoh model serves as a fundamental mathematical validation, it describes an idealized system with a harmonic core. To evaluate the spectral solver in a regime representative of massive early-type galaxies (ETGs)—characterized by high central concentrations and significant dark matter fractions—I construct a more realistic composite model.

I model the stellar tracer as an axisymmetric oblate distribution with an intrinsic axial ratio $q = 0.5$ and a Sérsic $n = 4$ profile ([de Vaucouleurs 1948](#)), typical for massive ETGs (see [Cappellari 2026](#)). The gravitational potential is generated by a total mass distribution following a generalized NFW (gNFW) profile ([Wyithe et al. 2001](#)). I approximate both the tracer and the total density with 20 Gaussians each, using the `MGE_FIT_1D` function of the `MGEFit` package² ([Cappellari 2002](#)). I adopt a total density inner slope of $\rho_{\text{tot}} \propto r^{-2.2}$, consistent with observations of massive ETGs out to several effective radii (e.g. [Cappellari et al. 2015](#); [Serra et al. 2016](#); [Bellstedt et al. 2018](#)).

The gNFW break radius is set to $r_s = 10 R_e$. This choice is motivated by the empirical relation between the stellar half-mass radius and halo size, $r_{1/2} \approx 0.015 R_{200}$ ([Kravtsov 2013](#)). Using the approximation $r_{1/2} \approx (4/3)R_e$ for a Sérsic $n = 4$ profile ([Ciotti 1991](#),

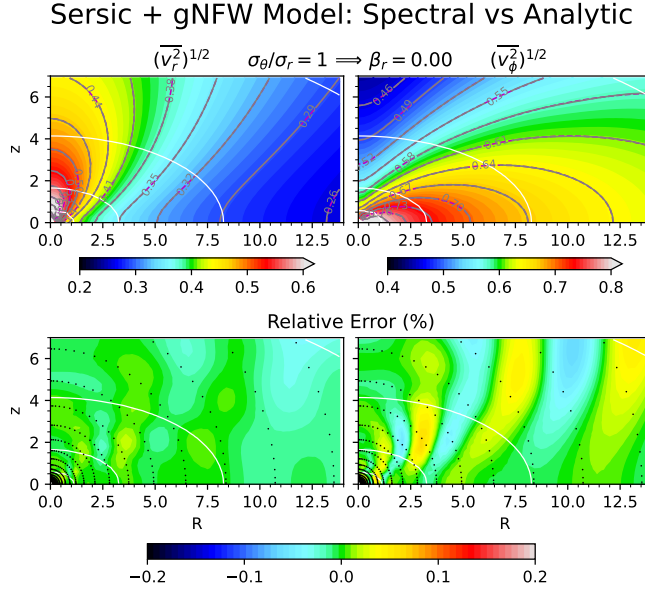


Figure 4. Validation of the spectral solver using a realistic composite galaxy model (Sérsic $n = 4$ stellar bulge and a cuspy gNFW dark matter halo with inner slope $\gamma = -2.2$). **Top panels:** Intrinsic radial and azimuthal velocity dispersion maps $(v_r^2)^{1/2}$ and $(v_\phi^2)^{1/2}$. **Bottom panels:** Relative percentage error between the spectral solution and the exact analytic MGE solution derived in Section A. Despite the high dynamic range and central cusp, the maximum error remains remarkably low (< 0.2 per cent).

Table 2), this relation can be rewritten as $r_s \approx 89 R_e / c_{200}$. For a representative halo concentration of $c_{200} \approx 9$ (e.g. Dutton & Macciò 2014), this yields $r_s \approx 10 R_e$. This scale is much larger than the typical field of view and ensures the test probes a regime where the potential has not yet reached its asymptotic Keplerian form.

This setup describes a non-self-consistent model where the stellar component acts as a tracer in a total potential that I assume to be spherical to provide an exact benchmark. This configuration is widely used in the dynamical modelling of real galaxies (e.g. Poci et al. 2017; Lu et al. 2024). Crucially, rather than comparing the spectral solution to a standard numerical integration, I compare it against the *analytic* solution for the Jeans equations of an MGE tracer in a spherical MGE potential, which I derive in Section A. By using identical MGE coefficients for both the solver and the analytic formulae, I isolate the discretization errors of the PDE solver from any errors associated with MGE fitting.

The results are presented in Fig. 4 and Fig. 5. Despite the high dynamic range of the $n = 4$ profile, the spectral method recovers the analytic solution with a maximum relative error of ~ 0.15 per cent. The convergence properties analysed in Fig. 5 confirm that the Robin boundary condition (equation (19)) restores exponential convergence, achieving a precision of $\sim 10^{-4}$ with a modest 30×15 grid. This confirms the method is robust for modelling realistic density profiles of galaxies with dark halos.

5.3 Comparison with numerical anisotropic JAM_{sph} solutions

In the general case of a Sérsic + gNFW model with non-zero anisotropy ($\beta \neq 0$), no analytic solution exists for the Jeans equations. To validate the spectral solver in this regime, I benchmark its performance against the standard public JAMPY code (Cappellari 2020). Specifically, I use the JAM_{sph} implementation, which utilizes a robust numerical

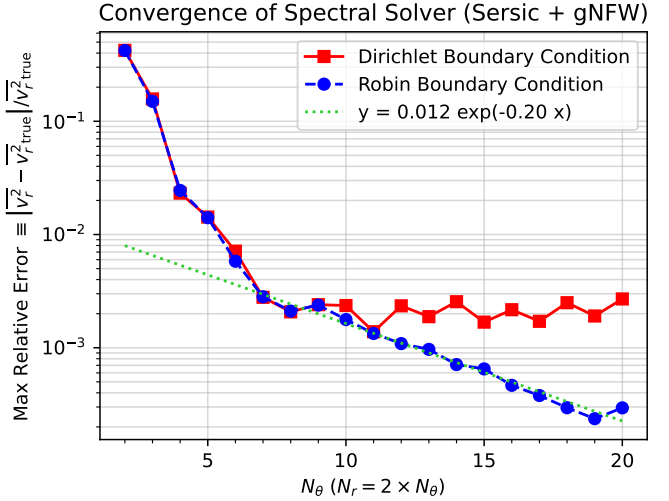


Figure 5. Numerical convergence analysis for the Sérsic + gNFW model. As observed in the Satoh test, the Dirichlet boundary condition (red squares) suffers from truncation errors that cause the accuracy to plateau. The Keplerian Robin boundary condition (blue circles) restores exponential convergence, reaching a precision of 10^{-4} . The slightly shallower slope relative to the Satoh case (Fig. 3) is expected given the steep density gradients inherent to the $n = 4$ profile and the gNFW cusp.

scheme based on a direct 2D quadrature of the Jeans equations for a spherically aligned velocity ellipsoid. To ensure that my reference model is more accurate than the spectral solver, I configure JAM_{sph} with quadrature with stringent relative error tolerance of $\epsilon = 10^{-4}$.

To probe the solver’s stability across different orbital regimes, I test two cases of constant anisotropy. These represent the extreme range of values found in observed galaxies (Cappellari 2026, fig. 10).

- (i) A radially anisotropic model with $\sigma_\theta/\sigma_r = 3/4$, yielding $\beta = 1 - (3/4)^2 \approx 0.44$.
- (ii) A tangentially anisotropic model with $\sigma_\theta/\sigma_r = 4/3$, yielding $\beta = 1 - (4/3)^2 \approx -0.78$.

The results are presented in Fig. 6. In both scenarios, the spectral method produces velocity fields that are virtually indistinguishable from the JAM_{sph} benchmarks. The relative differences are consistently below 0.2 per cent throughout the computational domain.

Because JAM_{sph} is itself a numerical implementation with its own convergence properties, this level of agreement confirms that the spectral solver correctly converges to the same physical solution within the accuracy limits of the reference code. This test successfully validates the implementation of the anisotropy terms and the coupling between the radial and angular components in the spectral formulation. These results demonstrate that the spectral solver can handle the range of orbital configurations typically required for the dynamical modelling of real galaxies.

5.4 Spectral JAM_{sph} with angular anisotropy variation

A key novelty of the spectral method presented here is its ability to handle a completely general anisotropy distribution $\beta(r, \theta)$ without compromising computational efficiency. This capability allows for models that are far more physically realistic than those limited by standard assumptions of constant anisotropy or rigid geometric alignments (spherical versus cylindrical).

This flexibility is illustrated in Fig. 7, where I use the spectral

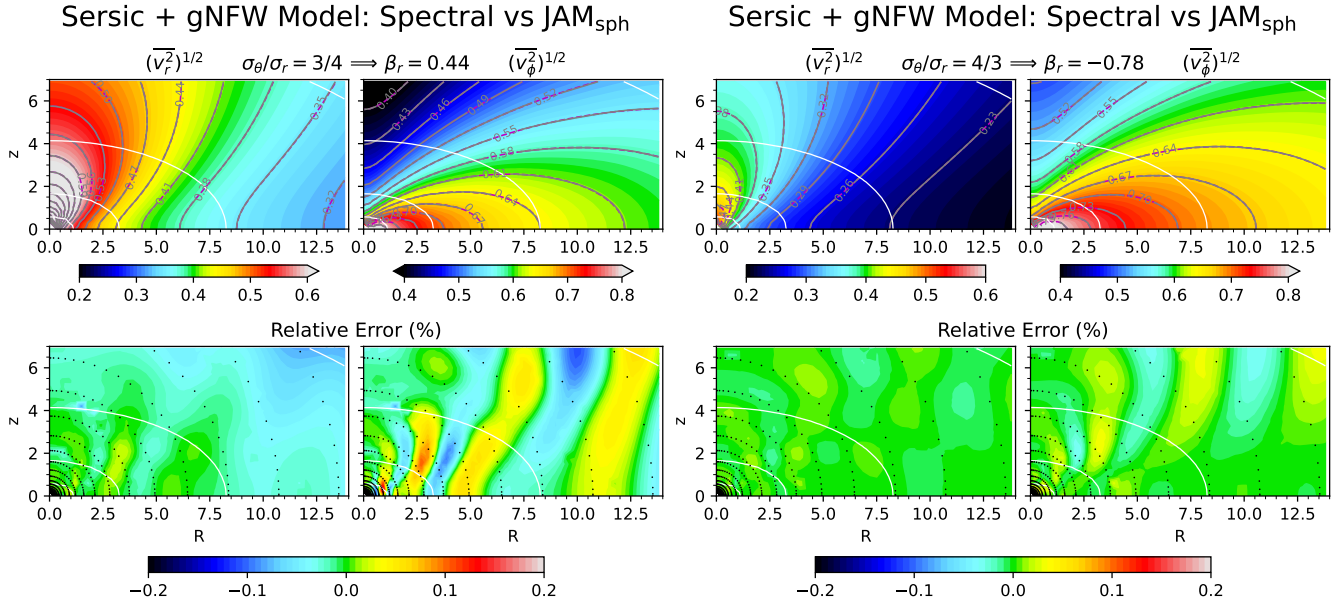


Figure 6. Comparison of the spectral solver against the standard JAM_{sph} numerical quadrature for the Sérsic + gNFW model with constant anisotropy. **Left panels:** Radially anisotropic case ($\beta \approx 0.44$, corresponding to $\sigma_\theta/\sigma_r = 0.75$). **Right panels:** Tangentially anisotropic case ($\beta \approx -0.78$, corresponding to $\sigma_\theta/\sigma_r = 1.33$). The top rows show the intrinsic velocity dispersions $(v_r^2)^{1/2}$ and $(v_\phi^2)^{1/2}$, while the bottom rows show the relative percentage errors. In both regimes, the discrepancy between the two numerical methods remains below 0.2 per cent.

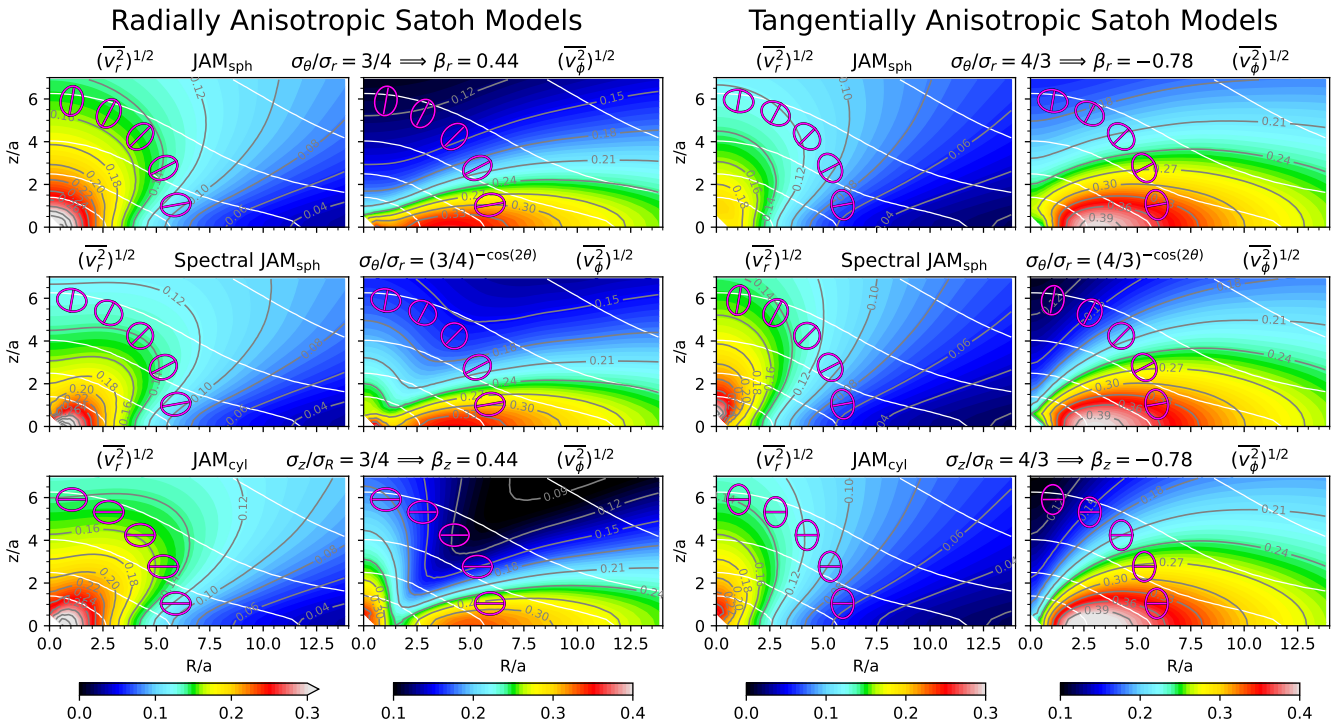


Figure 7. Comparison of velocity second moments under different anisotropy configurations for a Satoh model. **Left panels:** Radially anisotropic case ($\mathcal{R} = 3/4$). **Right panels:** Tangentially anisotropic case ($\mathcal{R} = 4/3$). **Top Row:** Standard JAM_{sph} with constant spherical anisotropy. The velocity ellipsoid orientation is fixed and strictly radial (pink ellipses). **Middle Row:** New Spectral JAM with angularly varying anisotropy $\beta_\theta(\theta) = 1 - \mathcal{R}^{-2\cos(2\theta)}$. This configuration mimics the varying shape of the velocity ellipsoid observed in realistic galaxies while maintaining a spherical coordinate framework. **Bottom Row:** Standard JAM_{cyl} with constant cylindrical anisotropy β_z . Note that the Spectral models (middle) successfully reproduce the global kinematic features of the Cylindrical models (bottom), which are known to characterize fast-rotators well. However, the Spectral models avoid the unphysical artifacts, such as the sharp drop in v_ϕ^2 near the rotation axis (dark region in bottom-left), providing a physically robust solution.

solver to approximate the complex anisotropy structure observed in real galaxies. As detailed in [Cappellari \(2008\)](#) and summarized in their fig. 1, the velocity ellipsoid of fast-rotator early-type galaxies is essentially aligned with the spherical coordinate system (r, θ, ϕ) everywhere. However, the axis of maximum elongation of the ellipsoid is not fixed relative to the radius vector. Instead, the shape of the ellipsoid varies with position: the major axis is radially aligned in the equatorial plane but becomes orthogonal to the radial direction (tangential) near the galaxy symmetry axis (the z -axis). This behaviour leads to a global anisotropy that, to first order, resembles a simple flattening of the velocity ellipsoid in the z -direction ($\overline{v_z^2} < \overline{v_R^2}$).

The cylindrically aligned JAM models (JAM_{cyl}) were originally designed as a simple and efficient heuristic to approximate this variation using a constant anisotropy in cylindrical coordinates ($\beta_z = 1 - \overline{v_z^2}/\overline{v_R^2}$). Here, I demonstrate that the spectral solver can reproduce this realistic behavior within a spherical alignment framework by adopting an angularly varying anisotropy parameter. I introduce a variation of the form:

$$\beta_\theta(\theta) = 1 - \mathcal{R}^{-2\cos(2\theta)}, \quad (32)$$

where \mathcal{R} is the anisotropy ratio parameter. This function ensures that the ratio of tangential to radial dispersion, σ_θ/σ_r , transitions smoothly from \mathcal{R} at the equatorial plane ($\theta = \pi/2$) to $1/\mathcal{R}$ at the symmetry axis ($\theta = 0$). This mimics the variation inherent in cylindrical models where the ratio σ_z/σ_R is roughly constant.

[Fig. 7](#) compares three scenarios using a Satoh model:

- (i) Standard JAM_{sph} with constant anisotropy (top row).
- (ii) The new Spectral JAM with the angular variation $\beta_\theta(\theta)$ described above (middle row).
- (iii) JAM_{cyl} with constant β_z (bottom row).

I test two ratios: $\mathcal{R} = 3/4$ (radially anisotropic at the equator) and $\mathcal{R} = 4/3$ (tangentially anisotropic at the equator). The similarity between the JAM_{cyl} models and the new spectral models is striking. This confirms that the success of cylindrical models in fitting fast-rotator kinematics (e.g. [Cappellari et al. 2007](#)) stems from their ability to capture these gross variations in orbital anisotropy.

However, the spectral models offer a crucial improvement. The JAM_{cyl} solution in the radially anisotropic case (bottom-left) exhibits a strong, artificial drop in $\overline{v_\phi^2}$ near the rotation axis (visible as a dark hole in the velocity map). This is a known unphysical artifact of the cylindrical approximation when β_z is large and positive. The spectral solution with angular β variation (middle-left) reproduces the correct global structure but remains free of such artifacts. Similarly, the spectral result for the tangentially anisotropic case (middle-right) is strikingly similar to the cylindrical counterpart (bottom-right). This test demonstrates the ability of the spectral method to provide physically robust solutions that accurately reflect the underlying dynamical processes, avoiding the singularities introduced by the cylindrical approximation and all without computation speed penalty.

The ability of this spectral solver to handle general $\beta(r, \theta)$ distributions, also makes it a valuable tool for testing and debugging orbit-superposition (Schwarzschild) codes. Specifically, one can construct a Jeans model with the same intrinsic second moments as those fitted by a Schwarzschild code on an (r, θ) grid. Since the spectral solution is accurate to numerical precision, it can be used to verify that the Schwarzschild code recovers the correct projected moments, thereby quantifying discretization errors in the orbit-integration or weight-solving stages.

5.5 Execution time benchmarks

Comparing the execution time of the spectral method against the standard quadrature approach is non-trivial due to their fundamentally different convergence properties. The spectral method yields a global solution with exponential convergence, whereas the standard method relies on independent point-wise quadratures controlled by a tolerance parameter. A rigorous comparison would require tuning the quadrature tolerance to match the *post hoc* accuracy of the spectral solution against an exact analytic benchmark.

Despite these caveats, a comparative test on identical hardware (an Intel Core i7-1355U CPU) provides a compelling illustration of the efficiency gains. I tested two grid configurations using the standard Python 3.13 implementation, based on the examples that produced [Fig. 6](#). For the standard JAMPy (version 8.1) benchmarks, I maintained a default relative precision of $\epsilon = 0.01$ for the JAM_{sph} quadrature (`epsrel=0.01`). In both cases, I computed the intrinsic moments ($\overline{v_r^2}, \overline{v_\phi^2}$) for the Sérsic + gNFW model with constant anisotropy $\beta \approx 0.44$ on a polar grid without subsequent interpolation:

- (i) **Standard resolution** ($N_r \times N_\theta = 20 \times 10$): This grid is the default for intrinsic moments in the public JAMPy package with semi-isotropic alignment (`align='sph'`). Comparing the spectral solver against a quadrature evaluation at these points yielded a speedup of $\approx 100\times$.
- (ii) **High resolution** ($N_r \times N_\theta = 32 \times 24$): On the finer grid used for the error maps in this paper, the spectral method scales more steeply due to the $O(N^3)$ cost of the linear algebra solver, compared to the $O(N)$ linear scaling of independent point-wise quadratures. Nevertheless, the speedup remains a substantial $\approx 80\times$.

It is important to emphasize that while the current Python implementations do not yet utilize specialized hardware features or explicit parallelism, the two methods were designed with different computational architectures in mind. The traditional quadrature method was primarily developed for scalar, single-threaded execution. In contrast, the spectral method was explicitly designed for massive parallelism, such as that provided by GPUs or modern multi-core CPUs. In the spectral approach, the bulk of the computation is consolidated into dense linear algebra operations (specifically matrix-matrix multiplications and system inversions), which are the types of tasks most effectively accelerated by parallel hardware.

These tests demonstrate that the spectral method provides a dramatic improvement in speed at comparable accuracy. In fact, the Jeans solution becomes so efficient that the computational bottleneck of the entire dynamical modelling procedure shifts to the subsequent step: the convolution of the projected moments with the Point Spread Function (PSF). Fortunately, Fourier convolutions can be performed extremely efficiently on specialized hardware (e.g. GPUs).

Because this acceleration removes the primary computational hurdle of the Jeans solver, it serves as a critical enabler for next-generation modelling pipelines. For this reason, I limit the benchmarks here to the intrinsic moments—the core novelty of this work—rather than characterizing the full forward-modelling execution time, which depends heavily on the implementation details of the convolution step.

Finally, it is worth noting that speeding up the solver is not the only strategy to accelerate parameter inference. When the parameter space is low-dimensional, one can effectively emulate the model likelihood via interpolation of a grid of pre-computed models (e.g. the analysis of [Tdcosmo Collaboration et al. 2025](#)). Similarly, machine learning techniques are increasingly being used as emulators to bypass direct equation solving, including specifically as a JAM emulator (e.g.

(Gomer et al. 2023; Simon et al. 2024a). However, these emulator approaches still require a fast and accurate solver to generate training data, and they become less feasible as the dimensionality of the model increases (e.g., when exploring the general anisotropy profiles enabled by this method). The spectral solver presented here thus complements these approaches by providing the fundamental speed and flexibility required for high-dimensional dynamical exploration.

6 CONCLUSIONS

In this paper, I have introduced a new spectral solver for the axisymmetric Jeans equations that overcomes the long-standing trade-off between computational speed and physical flexibility in dynamical modelling. By transforming the partial differential equations into a linear system using Chebyshev collocation, the method achieves a combination of generality and efficiency that was previously unattainable with standard integral-transform techniques.

The core innovations and results can be summarized as follows:

(i) **General Anisotropy:** Unlike the standard semi-analytic quadratures used in packages like JAMPY, which require specific integrability conditions, the spectral solver handles completely general anisotropy distributions $\beta(r, \theta)$. I demonstrated that this allows for the construction of physically motivated models—such as those with angularly varying anisotropy—that can reproduce the realistic kinematics of fast-rotator galaxies (e.g., mimicking cylindrical alignment) without introducing unphysical artifacts like the axial “holes” in velocity maps characteristic of the cylindrical approximation.

(ii) **Algorithmic Formulation:** The method solves directly for the intrinsic velocity second moment $\overline{v_r^2}$ rather than the pressure νv_r^2 . This choice minimizes the dynamic range of the solution, allowing for a compact spectral representation. Crucially, I implemented a Robin boundary condition that enforces asymptotic Keplerian decay. This effectively handles the infinite domain problem on a finite grid, preventing the error saturation associated with Dirichlet conditions and preserving the exponential convergence characteristic of spectral methods.

(iii) **Rigorous Validation:** The solver was benchmarked against two exact analytic solutions: the self-consistent Satoh (1980) model and a new analytic solution for an MGE tracer in a spherical MGE potential, derived in Appendix A. In both tests, the spectral method recovered the intrinsic moments with negligible errors (< 0.2 per cent), even in regimes featuring steep central cusps and high dynamic ranges typical of massive early-type galaxies. Further comparisons with the standard JAMPY quadrature code confirmed its accuracy for anisotropic models.

(iv) **Efficiency:** Despite its generality, the spectral method is orders of magnitude faster than traditional high-accuracy quadratures. It reduces the solution of the Jeans equations to standard linear algebra operations (matrix-vector products), making it naturally suited for massive parallelization on GPUs. This efficiency shifts the computational bottleneck of dynamical modelling from the Jeans solver to the PSF convolution step, paving the way for the next generation of Bayesian inference pipelines.

This solver enables the exploration of the full solution space allowed by the axisymmetric Jeans equations, facilitating rigorous parameter inference for complex galaxy models. A reference implementation of the spectral JAM method will be included in a future release of the public JAMPY package (Cappellari 2008, 2020).

ACKNOWLEDGEMENTS

I am grateful to the many users of the JAMPY package whose extensive feedback and challenging applications have pushed the limits of the software over the years. Their ambitious science cases were the primary motivation for developing this new solver.

DATA AVAILABILITY

No data were generated or analysed in this study. The code implementing the spectral JAM solver will be made publicly available in a future release of the JAM package (Cappellari 2008, 2020) at <http://pypi.org/project/jampy>.

REFERENCES

Arfken G. B., Weber H. J., Harris F. E., 2013, Mathematical Methods for Physicists (Seventh Edition). Academic Press, Boston, [doi:10.1016/C2009-0-30629-7](https://doi.org/10.1016/C2009-0-30629-7)

Arnold R., 1995, *MNRAS*, **276**, 293

Bacon R., 1985, *A&A*, **143**, 84

Bacon R., Simien F., Monnet G., 1983, *A&A*, **128**, 405

Bacon R., et al., 1995, *A&AS*, **113**, 347

Bellstedt S., et al., 2018, *MNRAS*, **476**, 4543

Berrut J.-P., Trefethen L. N., 2004, *SIAM Review*, **46**, 501

Binney J., 1981, *MNRAS*, **196**, 455

Binney J., 2012, *MNRAS*, **426**, 1324

Binney J., Tremaine S., 2008, *Galactic Dynamics*: Second Edition. Princeton University Press, Princeton, NJ, [doi:10.2307/j.ctvc778ff](https://doi.org/10.2307/j.ctvc778ff)

Binney J. J., Davies R. L., Illingworth G. D., 1990, *ApJ*, **361**, 78

Bovy J., 2015, *ApJS*, **216**, 29

Boyd J. P., 2001, Chebyshev and Fourier Spectral Methods, second revised edn. Dover Books on Mathematics, Dover Publications, Mineola, NY, https://openlibrary.org/books/OL6780843M/Chebyshev_and_Fourier_spectral_methods

Bundy K., et al., 2015, *ApJ*, **798**, 7

Canuto C., Hussaini M. Y., Quarteroni A., Zang T., eds, 2007, *Spectral Methods*. SpringerLink, Springer Berlin Heidelberg, Berlin, Heidelberg, [doi:10.1007/978-3-540-30728-0](https://doi.org/10.1007/978-3-540-30728-0)

Cappellari M., 2002, *MNRAS*, **333**, 400

Cappellari M., 2008, *MNRAS*, **390**, 71

Cappellari M., 2016, *ARA&A*, **54**, 597

Cappellari M., 2020, *MNRAS*, **494**, 4819

Cappellari M., 2026, in Mandel I., ed., , Vol. 4, *Encyclopedia of Astrophysics*, Volume 4. Elsevier, Amsterdam, The Netherlands, pp 122–152 ([arXiv:2503.02746](https://arxiv.org/abs/2503.02746)), [doi:10.1016/B978-0-443-21439-4.00109-7](https://doi.org/10.1016/B978-0-443-21439-4.00109-7)

Cappellari M., et al., 2007, *MNRAS*, **379**, 418

Cappellari M., et al., 2011, *MNRAS*, **413**, 813

Cappellari M., et al., 2015, *ApJ*, **804**, L21

Ciotti L., 1991, *A&A*, **249**, 99

Croom S. M., et al., 2012, *MNRAS*, **421**, 872

Dejonghe H., de Zeeuw T., 1988, *ApJ*, **333**, 90

Dutton A. A., Macciò A. V., 2014, *MNRAS*, **441**, 3359

Eddington A. S., 1915, *MNRAS*, **76**, 37

Emsellem E., Monnet G., Bacon R., 1994, *A&A*, **285**, 723

Evans N. W., 1990, *International Journal of Computer Mathematics*, **34**, 105

Evans N. W., 1993, *MNRAS*, **260**, 191

Evans N. W., Lynden-Bell D., 1991, *MNRAS*, **251**, 213

Evans N. W., de Zeeuw P. T., 1994, *MNRAS*, **271**, 202

Evans N. W., Sanders J. L., Williams A. A., An J., Lynden-Bell D., Dehnen W., 2016, *MNRAS*, **456**, 4506

Everall A., Evans N. W., Belokurov V., Schönrich R., 2019, *MNRAS*, **489**, 910

Gaia Collaboration et al., 2016, *A&A*, **595**, A1

Gomer M. R., et al., 2023, *A&A*, **679**, A59

Hagen J. H. J., Helmi A., de Zeeuw P. T., Posti L., 2019, [A&A](#), **629**, A70

Hernquist L., 1990, [ApJ](#), **356**, 359

Hunt J. A. S., Vasiliev E., 2025, [New Astron. Rev.](#), **100**, 101721

Jeans J. H., 1922, [MNRAS](#), **82**, 122

Jin Y., Zhu L., Long R. J., Mao S., Xu D., Li H., van de Ven G., 2019, [MNRAS](#), **486**, 4753

Jones E., Oliphant T., Peterson P., et al., 2001, SciPy: Open source scientific tools for Python, <http://www.scipy.org/>

Kravtsov A. V., 2013, [ApJ](#), **764**, L31

Leung G. Y. C., et al., 2018, [MNRAS](#), **477**, 254

Lu S., Zhu K., Cappellari M., Li R., Mao S., Xu D., 2024, [MNRAS](#), **530**, 4474

Miyamoto M., Nagai R., 1975, [PASJ](#), **27**, 533

Nagai R., Miyamoto M., 1976, [PASJ](#), **28**, 1

Navarro J. F., Frenk C. S., White S. D. M., 1996, [ApJ](#), **462**, 563

Owen D. B., 1956, [The Annals of Mathematical Statistics](#), **27**, 1075

Patefield M., Tandy D., 2000, [Journal of Statistical Software](#), **5**

Poci A., Cappellari M., McDermid R. M., 2017, [MNRAS](#), **467**, 1397

Press W. H., Teukolsky S. A., Vetterling W. T., Flannery B. P., 2007, Numerical recipes: The art of scientific computing, 3rd edn. Cambridge Univ. Press, Cambridge, <http://numerical.recipes/book>

Sánchez S. F., et al., 2012, [A&A](#), **538**, A8

Satoh C., 1980, [PASJ](#), **32**, 41

Schwartz C., 1969, [Journal of Computational Physics](#), **4**, 19

Schwarzschild M., 1979, [ApJ](#), **232**, 236

Serra P., Oosterloo T., Cappellari M., den Heijer M., Józsa G. I. G., 2016, [MNRAS](#), **460**, 1382

Sérsic J. L., 1968, Atlas de galaxias australes. Obs. Astron. Univ. Nacional de Córdoba., Córdoba (translation at <https://doi.org/10.5281/zenodo.2562394>)

Shen J., Tang T., Wang L.-L., 2011, Spectral Methods: Algorithms, Analysis and Applications. Springer Berlin Heidelberg, doi:10.1007/978-3-540-71041-7

Simon D., Cappellari M., Mao S., 2024a, in EAS2024, European Astronomical Society Annual Meeting. p. 1323

Simon D. A., Cappellari M., Hartke J., 2024b, [MNRAS](#), **527**, 2341

Smet C. O., Posacki S., Ciotti L., 2015, [MNRAS](#), **448**, 2921

Strauss W. A., 2008, Partial differential equations, 2. ed. edn. Wiley, Hoboken, NJ, <https://openlibrary.org/books/OL10278713M>

Takahasi H., Mori M., 1974, [Publications of the Research Institute for Mathematical Sciences](#), **9**, 721

Tdcosmo Collaboration et al., 2025, [A&A](#), **704**, A63

Trefethen L. N., 2000, Spectral Methods in MATLAB. Society for Industrial and Applied Mathematics, doi:10.1137/1.9780898719598

Trefethen L. N., Weideman J. A. C., 2014, [SIAM Review](#), **56**, 385

Tremaine S., Richstone D. O., Byun Y.-I., Dressler A., Faber S. M., Grillmair C., Kormendy J., Lauer T. R., 1994, [AJ](#), **107**, 634

Vasiliev E., 2019, [MNRAS](#), **482**, 1525

Wegg C., Gerhard O., Bieth M., 2019, [MNRAS](#), **485**, 3296

Wolfram S., 2003, The Mathematica Book, 5th ed.. Wolfram Media, Champaign, IL, <http://reference.wolfram.com/>

Wyithe J. S. B., Turner E. L., Spergel D. N., 2001, [ApJ](#), **555**, 504

Yurin D., Springel V., 2014, [MNRAS](#), **444**, 62

Zhao H., 1996, [MNRAS](#), **278**, 488

de Vaucouleurs G., 1948, [Annales d’Astrophysique](#), **11**, 247

de Zeeuw T., 1985, [MNRAS](#), **216**, 273

de Zeeuw P. T., Evans N. W., Schwarzschild M., 1996, [MNRAS](#), **280**, 903

van de Ven G., Hunter C., Verolme E. K., de Zeeuw P. T., 2003, [MNRAS](#), **342**, 1056

van der Marel R. P., 1991, [MNRAS](#), **253**, 710

APPENDIX A: ANALYTIC AXISYMMETRIC MGE JEANS SOLUTION IN A SPHERICAL POTENTIAL

To rigorously benchmark the numerical accuracy of the spectral Jeans Anisotropic Multi-Gaussian Expansion (JAM) method, it is essential to compare its results against exact solutions that share the

same underlying physical assumptions. However, analytic solutions to the two-integral or semi-isotropic Jeans equations for non-spherical systems are relatively rare.

Historically, the Jeans equations, in the isotropic limit, have been solved analytically for several self-consistent axisymmetric models—where the gravitational potential is derived directly from the density distribution. Notable examples include the Miyamoto & Nagai (1975) model, with its corresponding Jeans solution provided by Nagai & Miyamoto (1976), and the Satoh (1980) model utilized in the main body of this paper. A comprehensive review of such analytic isotropic Jeans solutions can be found in Smet et al. (2015). More complex isotropic Jeans solutions for non-self-consistent or composite models, which are capable of describing galaxies embedded in dark matter halos, are even less common. Examples of these include axisymmetric power-law densities within the logarithmic potential of Binney (1981) solved by Evans (1993); Evans & de Zeeuw (1994). Perhaps the most physically realistic analytic benchmark currently available is the axisymmetric isotropic Miyamoto–Nagai tracer embedded in a logarithmic potential (Smet et al. 2015).

Standard analytic tests, such as those employing the Satoh (1980) model, typically require approximating the density distributions using a Multi-Gaussian Expansion (MGE). This introduces an unavoidable fitting error that can obscure the intrinsic precision of the Jeans solver itself. The derivation presented in this Appendix circumvents this issue by providing a fully analytic solution to the cylindrically-aligned Jeans equations for a flattened axisymmetric MGE tracer embedded in a spherical MGE potential.

This formulation offers several distinct advantages for code validation:

(i) **Elimination of Fitting Bias:** Since both the tracer density and the gravitational potential are defined exactly as a sum of Gaussians, the analytic solution uses the precise input parameterization required by the numerical JAM solver. Any resulting discrepancies must, therefore, stem from the numerical scheme or the quadrature accuracy rather than MGE approximation errors.

(ii) **Physical Realism:** While this configuration is not strictly self-consistent—due to the use of a spherical potential rather than a flattened one—it remains highly relevant. In real galaxies, the gravitational potential is significantly rounder than the underlying mass distribution (e.g. Fig. 2.14 of Binney & Tremaine 2008). Jeans models using circularized potentials are known to provide excellent qualitative and quantitative descriptions of isotropic solutions in realistic galaxies, provided the tracer remains properly axisymmetric.

(iii) **Generality:** Given the flexibility of the MGE method to accurately fit almost any arbitrary galaxy profile, this derivation allows for the analytic computation of the Jeans equations for nearly any combination of tracer and dark matter density.

Consequently, this solution serves as a highly valuable and flexible testbed for validating the next generation of numerical Jeans solvers.

A1 The vertical velocity dispersion v_z^2

Following the assumptions of Cappellari (2008, sec. 3.1), I consider an axisymmetric system where both the dynamical tracer population and the total mass density are parameterized via the Multi-Gaussian Expansion (MGE). I further assume a cylindrically-aligned velocity ellipsoid.

For a single axisymmetric Gaussian tracer component k , defined by peak density $\nu_{0,k}$, radial dispersion σ_k , and intrinsic flattening q_k ,

the density distribution is:

$$\nu_k(R, z) = \nu_{0,k} \exp \left[-\frac{R^2}{2\sigma_k^2} - \frac{z^2}{2(q_k \sigma_k)^2} \right]. \quad (\text{A1})$$

The gravitational potential Φ is generated by a sum of spherical Gaussian mass components j , each with total mass M_j and dispersion σ_j . Imposing the boundary condition $\nu_k \overline{v_{z,k}^2} \rightarrow 0$ as $z \rightarrow \infty$, the vertical Jeans equation is (Binney & Tremaine 2008, eq. 4.223):

$$\nu_k(R, z) \overline{v_{z,k}^2}(R, z) = \int_z^\infty \nu_k(R, z') \frac{\partial \Phi}{\partial z'} dz'. \quad (\text{A2})$$

By defining the vertical scale length of the tracer as $\sigma_{z,k} \equiv q_k \sigma_k$, a crucial mathematical simplification emerges: the radial dependent factor $f(R) = \exp[-R^2/(2\sigma_k^2)]$ appears on both sides of [equation \(A2\)](#) and cancels out completely. This reduction leaves an expression dependent only on the vertical coordinate z and the spherical potential $\Phi(r)$, where $r = \sqrt{R^2 + z^2}$:

$$\overline{v_{z,k}^2} = \exp \left(\frac{z^2}{2\sigma_{z,k}^2} \right) \int_z^\infty \exp \left(-\frac{z'^2}{2\sigma_{z,k}^2} \right) \frac{\partial \Phi}{\partial z'} dz'. \quad (\text{A3})$$

For a spherical Gaussian mass component j , the vertical force is given by $\partial \Phi_j / \partial z' = (GM_j / r^3)z'$. I now perform a change of variable from the vertical coordinate z' to the spherical radius r (noting that $r dr = z' dz'$). This transforms the integration limits from $z' \in [z, \infty)$ to $r' \in [r, \infty)$, where $r = \sqrt{R^2 + z^2}$. The exponential kernel transforms as:

$$\exp \left(-\frac{z'^2}{2\sigma_{z,k}^2} \right) = \exp \left(\frac{R^2}{2\sigma_{z,k}^2} \right) \exp \left(-\frac{r'^2}{2\sigma_{z,k}^2} \right). \quad (\text{A4})$$

Extracting the constant factor $\exp[R^2/(2\sigma_{z,k}^2)]$ from the integral and combining it with the prefactor $\exp[z^2/(2\sigma_{z,k}^2)]$ yields $\exp[r^2/(2\sigma_{z,k}^2)]$. Consequently, the resulting second velocity moment $\overline{v_{z,k}^2}$ becomes a function of the spherical radius r alone:

$$\overline{v_{z,k}^2}(r) = \exp \left(\frac{r^2}{2\sigma_{z,k}^2} \right) \int_r^\infty \exp \left(-\frac{r'^2}{2\sigma_{z,k}^2} \right) \frac{GM_j(r')}{r'^2} dr', \quad (\text{A5})$$

where the enclosed mass for the spherical Gaussian component j is (Cappellari 2008, eq. 49):

$$M_j(r) = M_j \left[\text{erf} \left(\frac{r}{\sqrt{2}\sigma_j} \right) - \sqrt{\frac{2}{\pi}} \frac{r}{\sigma_j} \exp \left(-\frac{r^2}{2\sigma_j^2} \right) \right]. \quad (\text{A6})$$

The integral in [equation \(A5\)](#) is mathematically equivalent to the solution for a spherical MGE with isotropic radial dispersion, but with the tracer's vertical dispersion $\sigma_{z,k}$ substituted for σ_k . By utilizing the identity $\int \exp(-Ct^2) dt / (1 + t^2) \propto \text{erf} - \exp(C)T(\dots)$, the final analytic solution for a single tracer component k interacting with a single potential component j is:

$$\overline{v_{z,k}^2}(r) = GM_j \left[\frac{1}{r} \text{erf} \left(\frac{r}{\sqrt{2}\sigma_j} \right) - \frac{\sqrt{8\pi}}{\sigma_{z,k}} \exp \left(-\frac{r^2}{2\sigma_{z,k}^2} \right) T \left(\frac{r}{\sigma_{z,k}}, \frac{\sigma_{z,k}}{\sigma_j} \right) \right], \quad (\text{A7})$$

where $T(\cdot, \cdot)$ is Owen's T function (Owen 1956). This function is readily available in standard numerical libraries, such as `scipy.special.owens_t` in Python (Jones et al. 2001), following the implementation by Patefield & Tandy (2000), or the built-in `OwensT` in Mathematica (Wolfram 2003).

Since the gravitational potential is additive, the velocity second moment for a specific tracer component k corresponds to the sum of

the contributions from all M Gaussian components of the potential. To obtain the total velocity moments for the full MGE model, the second moments (either $\overline{v_z^2}$ or $\overline{v_\phi^2}$) are then calculated as the density-weighted average over all N tracer components:

$$\overline{v^2} = \frac{\sum_{k=1}^N \nu_k \left(\sum_{j=1}^M \overline{v_k^2} \right)_j}{\sum_{k=1}^N \nu_k}. \quad (\text{A8})$$

It is important to note that while the vertical dispersion of an individual Gaussian component $\overline{v_{z,k}^2}$ depends only on the radius r , the total dispersion $\overline{v_z^2}$ —obtained by summing over all tracer and potential components—will exhibit a full (R, z) dependence due to the varying vertical dispersions $\sigma_{z,k}$ of the different tracer components.

A2 Asymptotic expression to prevent numerical overflow

The analytic solution for $\overline{v_{z,k}^2}(r)$ in [equation \(A7\)](#) contains an exponential term $\exp[r^2/(2\sigma_{z,k}^2)]$ that can cause numerical overflow when the radius r is much larger than the tracer's vertical scale $\sigma_{z,k}$. In this regime, one might consider a point-mass approximation; however, such an approximation is only valid when r is large compared to *all* relevant length scales, including the dispersion σ_j of every Gaussian component in the potential. In realistic galaxy models, a tracer often resides at a radius r that is large compared to its $\sigma_{z,k}$ but still comparable to or smaller than the σ_j of the dark halo components.

To ensure numerical stability in this specific regime, I adopt an alternative expansion. Starting from the integral in [equation \(A5\)](#) and substituting the enclosed mass $M_j(r)$ from [equation \(A6\)](#), the dispersion can be rewritten as:

$$\overline{v_{z,k}^2}(r) = \frac{\sqrt{2} GM_j}{\sqrt{\pi} \sigma_{z,k}} \int_0^{\sigma_{z,k}/\sigma_j} \exp \left(-\frac{r^2 t^2}{2\sigma_{z,k}^2} \right) \frac{t^2}{1+t^2} dt. \quad (\text{A9})$$

When $r \gg \sigma_{z,k}$, the exponential kernel strongly suppresses the integrand for $t \gtrsim \sigma_{z,k}/r$, meaning the integral is dominated by the behavior near $t = 0$. In this limit, the rational factor can be expanded as a power series:

$$\frac{t^2}{1+t^2} = \sum_{n=1}^{\infty} (-1)^{n-1} t^{2n}. \quad (\text{A10})$$

Numerical tests confirm that the analytic solution in [equation \(A7\)](#) remains highly accurate and matches direct numerical quadrature until the point of floating-point overflow. Consequently, an asymptotic treatment is only necessary in the extreme regime where $r \gg \sigma_{z,k}$. In this limit, it is sufficient to retain only the leading-order term ($n = 1$) of the expansion.

Using the same notation as [equation \(A7\)](#), the leading-order approximation for $r \gg \sigma_{z,k}$ can be expressed in closed form as:

$$\overline{v_{z,k}^2}(r) \simeq \frac{GM_j \sigma_{z,k}^2}{r^2} \left[\frac{1}{r} \text{erf} \left(\frac{r}{\sqrt{2}\sigma_j} \right) - \sqrt{\frac{2}{\pi}} \frac{1}{\sigma_j} \exp \left(-\frac{r^2}{2\sigma_j^2} \right) \right]. \quad (\text{A11})$$

The corrections to this expression are of order $(\sigma_{z,k}/r)^2$ and are negligible in the regime where overflow occurs. Crucially, this expression remains valid even if r is not large compared to σ_j , making it robust for composite galaxy models.

A3 The azimuthal velocity second moment $\overline{v_\phi^2}$

For a cylindrically-aligned model where the radial and vertical second moments are related by $\overline{v_R^2} = b \overline{v_z^2}$ or equivalently $\beta_z = 1 - \overline{v_z^2}/\overline{v_R^2}$,

the semi-isotropic Jeans equation for the azimuthal second moment (Cappellari 2008, eq. 11) is given by:

$$\overline{v_{\phi,k}^2} = b \left[\overline{v_{z,k}^2} + \frac{R}{v_k} \frac{\partial(v_k \overline{v_{z,k}^2})}{\partial R} \right] + R \frac{\partial \Phi}{\partial R}. \quad (\text{A12})$$

To solve this analytically, I first expand the second term using the product rule:

$$\frac{R}{v_k} \frac{\partial(v_k \overline{v_{z,k}^2})}{\partial R} = R \frac{\partial \overline{v_{z,k}^2}}{\partial R} + \frac{R}{v_k} \overline{v_{z,k}^2} \frac{\partial v_k}{\partial R}. \quad (\text{A13})$$

From the tracer density defined in equation (A1), the logarithmic radial derivative is $\frac{\partial \ln v_k}{\partial R} = -R/\sigma_k^2$. Substituting this into the expansion and then into equation (A12) yields:

$$\overline{v_{\phi,k}^2} = b \overline{v_{z,k}^2} \left(1 - \frac{R^2}{\sigma_k^2} \right) + R \left(b \frac{\partial \overline{v_{z,k}^2}}{\partial R} + \frac{\partial \Phi}{\partial R} \right). \quad (\text{A14})$$

Since $\overline{v_{z,k}^2}$ is solely a function of the spherical radius r , its partial derivative with respect to R is $\partial \overline{v_{z,k}^2} / \partial R = (R/r) \partial \overline{v_{z,k}^2} / \partial r$. We can determine this derivative by invoking the radial Jeans equation for a purely spherical system in equilibrium:

$$\frac{d \overline{v_{z,k}^2}}{dr} = -\frac{d\Phi}{dr} - \frac{\overline{v_{z,k}^2}}{v_k} \frac{dv_k}{dr}. \quad (\text{A15})$$

For a spherical Gaussian tracer with $v_k \propto \exp[-r^2/(2\sigma_{z,k}^2)]$, the density gradient is $\frac{1}{v_k} \frac{dv_k}{dr} = -r/\sigma_{z,k}^2$. Thus:

$$\frac{d \overline{v_{z,k}^2}}{dr} = -\frac{d\Phi}{dr} + \frac{r}{\sigma_{z,k}^2} \overline{v_{z,k}^2}. \quad (\text{A16})$$

Substituting this result back into equation (A14), and noting that for a spherical potential $\partial\Phi/\partial R = (R/r)d\Phi/dr$, we have:

$$\overline{v_{\phi,k}^2} = b \overline{v_{z,k}^2} \left(1 - \frac{R^2}{\sigma_k^2} \right) + \frac{R^2}{r} \left[b \left(-\frac{d\Phi}{dr} + \frac{r}{\sigma_{z,k}^2} \overline{v_{z,k}^2} \right) + \frac{d\Phi}{dr} \right]. \quad (\text{A17})$$

By grouping the terms and substituting the gravitational force $d\Phi/dr = GM_j(r)/r^2$, where $M_j(r)$ is given by equation (A6), we arrive at the final analytic solution:

$$\overline{v_{\phi,k}^2}(R, z) = b \overline{v_{z,k}^2}(r) \left[1 + \frac{(1 - q_k^2)R^2}{\sigma_{z,k}^2} \right] + (1 - b) \frac{GM_j(r)R^2}{r^3}. \quad (\text{A18})$$

In the isotropic case ($b = 1$), the term proportional to the potential gradient vanishes, and the azimuthal moment becomes a simple scaled version of the vertical moment. This derivation highlights that even in a spherical potential, the flattening of the tracer distribution (q_k) explicitly couples the radial and vertical coordinates in the azimuthal velocity field.

A4 Contribution of a central black hole

Due to the linearity of the Jeans equations with respect to the gravitational potential Φ , the contribution of a central supermassive black hole of mass M_\bullet to the velocity second moments can be computed independently and added to the contribution from the total mass distribution.

For a point-mass potential $\Phi_\bullet = -GM_\bullet/r$, the integral for the vertical velocity dispersion (equation (A5)) can be solved analytically.

For a single Gaussian tracer component k , the BH-induced vertical second moment is given by (Emsellem et al. 1994, eq. 88):

$$\left[\overline{v_{z,k}^2} \right]_\bullet = \frac{GM_\bullet}{r} \left[1 - \sqrt{\frac{\pi}{2}} \frac{r}{\sigma_{z,k}} \text{erfcx} \left(\frac{r}{\sqrt{2}\sigma_{z,k}} \right) \right], \quad (\text{A19})$$

where $\text{erfcx}(x) = \exp(x^2) \text{erfc}(x)$ is the scaled complementary error function (scipy.special.erfcx in Scipy, Jones et al. 2001). This function is standard in many numerical libraries and is essential for avoiding arithmetic overflow when evaluating the term $\exp[\dots] \text{erfc}[\dots]$ at large radii.

The corresponding contribution to the azimuthal second moment is obtained by applying the BH radial force, $\partial\Phi_\bullet/\partial R = GM_\bullet R/r^3$, to the general solution in equation (A18):

$$\left[\overline{v_{\phi,k}^2} \right]_\bullet = b \left[\overline{v_{z,k}^2} \right]_\bullet \left[1 + \frac{(1 - q_k^2)R^2}{\sigma_{z,k}^2} \right] + (1 - b) \frac{GM_\bullet R^2}{r^3}. \quad (\text{A20})$$

This expression reduces to eq. (102) of Emsellem et al. (1994) in the isotropic case ($b = 1$).

The contribution due to the BH must be quadratically summed with the contributions from the extended mass components to obtain the total second moments.